ADVANCES IN ATMOSPHERIC SCIENCES, VOL. 42, APRIL 2025, 794–815

• **Original Paper** •

Ensemble-Based Adaptive Observations for Improving Sea Fog Prediction in Coastal Regions around the Bohai Sea: Case Study with Cold-Front Synoptic Pattern

Huiqin HU[1], Chengqing RUAN[*2], and Xiaolin YU[3]

[1]*Qingdao University of Science and Technology*, *Qingdao* 266061, *China*
[2]*North China Sea Marine Forecasting Center of State Oceanic Administration*, *Qingdao* 266033, *China*
[3]*Ocean University of China*, *Qingdao* 266100, *China*

(Received 5 December 2023; revised 8 May 2024; accepted 3 June 2024)

ABSTRACT

This study explored the observation strategy and effectiveness of synoptic-scale adaptive observations for improving sea fog prediction in coastal regions around the Bohai Sea based on a poorly predicted fog event with cold-front synoptic pattern (CFSP). An ensemble Kalman filter data assimilation system for the Weather Research and Forecasting model was adopted with ensemble sensitivity analysis (ESA). By comparing observation impacts (estimated from a 40-member ensemble with ESA) among different meteorological observation variables and pressure levels, the temperature at 850 hPa and surface layer (850 hPa-and-surface temperature) was selected as the target observation type. Additionally, the area with large observation impacts for this observation type was predicted in the transition region of the surface low–high system. This area developed southward with the low and moved eastward with the low–high system, which could be explained by the main features of CFSP. Moreover, both experiments assimilating synthetic and real observations showed that assimilating 850 hPa-and-surface temperature observations generally yielded better fog coverage forecasts in areas with greater observation impacts than areas with smaller impacts. However, the effectiveness of adaptive observations was reduced when real observations rather than synthetic observations were assimilated, which is possibly due to factors such as observation and model errors. The main conclusions above were verified by another typical fog event with CFSP characteristics. Results of this study highlight the importance of improved initial conditions in the transition region of the low–high system for improving fog prediction and provide scientific guidance for implementing an observation network for fog forecasting over the Bohai Sea.

Key words: sea fog forecasting, synoptic-scale adaptive observations, ESA method, observations of temperature profile below 850 hPa, cold-front synoptic pattern

Citation: Hu, H. Q., C. Q. Ruan, and X. L. Yu, 2025: Ensemble-based adaptive observations for improving sea fog prediction in coastal regions around the Bohai Sea: Case study with cold-front synoptic pattern. *Adv. Atmos. Sci.*, **42**(4), 794–815, https://doi.org/10.1007/s00376-024-3360-2.

Article Highlights:

- The effectiveness of target observation for fog forecasts were investigated.
- Temperature profile in target areas yielded better fog forecasts than other areas.

1. Introduction

Fog is a weather phenomenon that causes a reduction in the horizontal atmospheric visibility to below 1 km due to an abundance of tiny water droplets or ice crystals suspended in the boundary layer (Glickman, 2000). Sea fog is a type of fog that occurs at sea or in coastal regions (Li et al., 2012). Sea fog exerts a notable adverse impact on transportation (i.e., air, marine, and road traffic). For example, the Chinese Snow Dragon scientific research ship collided with an iceberg in the Amundsen Sea on 19 January 2019 because of dense sea fog. In regions with a high frequency of fog occurrence and heavy sea traffic, such as the coastal regions around the Bohai Sea (including Beijing, Tianjin, Hebei, and Shandong; Fig. 1), sea fog has become a high-impact weather phenomenon. Accurate numerical predictions of sea fog are therefore of increasing interest.

However, current accuracy of sea fog forecasting is still severely impaired by inaccurate model initial conditions (ICs), although assimilating existing conventional observations as well as satellite data or derived information has signif-

* Corresponding author: Chengqing RUAN
Email: ruanchq@hotmail.com

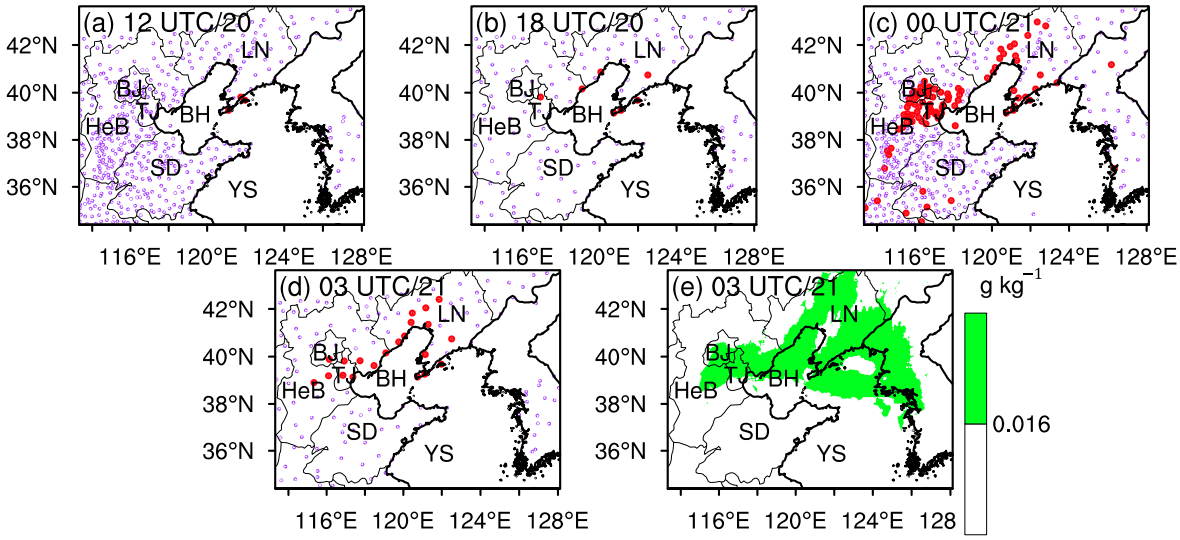

Fig. 1. (a–d) Observed fog coverage, defined as the area of points with a surface visibility ⩽ 1 km, from surface visibility observations (dots) obtained from the meteorological network of the China Meteorological Administration at 1200 UTC and 1800 UTC 20 February, and 0000 UTC and 0300 UTC 21 February 2007, respectively. Red and purple dots denote points with observed visibility for the range of ⩽ 1 km and > 1 km, respectively. (e) Observed fog coverage (shading) derived from Multifunctional Transport Satellite (MTSAT) data at 0300 UTC 21 February 2007. Abbreviations: BJ, Beijing; TJ, Tianjin; HeB, Hebei Province; SD, Shandong Province; LN, Liaoning Province; BH, Bohai Sea; YS, Yellow Sea.

icantly improved ICs for sea fog forecasting (Wang et al., 2014; Hu et al., 2017a, b, 2019; Yang et al., 2021). This implies that improving ICs by assimilating appropriate supplementary observations can potentially have benefits for accurate sea fog prediction. Because supplementary observations are costly, especially over the sea, observation strategies are urgently needed to determine the necessary types of observations and where to deploy them.

Adaptive observation is one such strategy, which aims to maximize the reduction in the forecast uncertainty of a numerical prediction model by obtaining supplemental observations in areas where further observations could likely improve forecasting (Palmer et al., 1998; Langland, 2005). Over the past few decades, adaptive observations have been widely used in the atmospheric sciences and have generated notable benefits in terms of improved numerical weather predictions, such as forecasts of precipitation, snow, storms, and tropical cyclones (TCs) (Morss et al., 2001; Xie et al., 2013; Huang and Meng, 2014). These studies indicate that adaptive observation is a potential method to improve sea fog forecasting. However, systematic research on adaptive observation in sea fog forecasting has not yet been conducted.

A key issue in adaptive observation is determining adaptive locations for targeting. Sensitivity analysis, which is aimed at evaluating how observation changes in ICs affect forecasts, could provide the basis to determine adaptive locations (Majumdar et al., 2011; Mu et al., 2015; Majumdar, 2016). Adaptive observation methods based on sensitivity analysis can be divided into adjoint- and ensemble-based techniques (Bishop and Toth, 1999; Buizza and Montani, 1999; Langland et al., 1999; Ancell and Hakim, 2007). Compared to adjoint-based techniques, which use the adjoint of a linearized forecast model, ensemble-based techniques, which use sample statistics, are much easier to implement (Torn and Hakim, 2008). Examples of ensemble-based sensitivity analysis methods include the ensemble transform method, which transforms the perturbations in the analysis ensemble at the target time to produce an estimate of the forecast error variance at the verification time (Bishop and Toth, 1999; Zhang et al., 2016), and the ensemble sensitivity analysis (ESA) method, which aims to calculate the linear regression of analysis errors at the target time onto a given forecast metric at the verification time (Ancell and Hakim, 2007; Torn and Hakim, 2008). Compared to the ensemble transform method, the ESA method shows benefits from considering the impact of observations on the analysis/forecast results when identifying adaptive locations (Ancell and Hakim, 2007).

With the use of the ESA method, Bei et al. (2012) explored the impact of adaptive observation on ozone prediction in Houston, Texas, USA, and the surrounding area with meteorological–photochemical coupled models. Subsequently, Xie et al. (2013) explored the observation strategy and observation targeting for the prediction of Typhoon Morakot (2009) with the Weather Research and Forecasting (WRF) model. Both studies showed that assimilating observations at identified adaptive locations generally provided a better forecast performance than assimilating observations at non-adaptive locations. Their results also indicated that the effectiveness of adaptive observation using the ESA method was limited. Given that the improvement of typhoon prediction

due to the linear improvement of moist convection (the governing dynamic) in ICs is sudden (Zhang and Sippel, 2009), and the ESA method is based on a linear theory that connects forecast changes to changes in ICs (Torn and Hakim, 2008), Xie et al. (2013) pointed out that the limited effectiveness of adaptive observation is possible due to the nonlinearity in the governing dynamics of the considered systems.

Mu (2013) highlighted that it is necessary to study adaptive observation from the perspective of synoptic-scale circulation, as it can help us make early decisions on whether to implement adaptive observations. Huang et al. (2011) and Wang (1983) reported that sea fog is closely associated with specific synoptic-scale circulations, and a common synoptic-scale circulation favorable for fog formation and maintenance over the Bohai Sea is the cold-front synoptic pattern (CFSP; see section 3.1). A dense fog event (hereafter referred to as the 2007 fog case; see section 3.1) with features typical of the CFSP occurred in the coastal region of the Bohai Sea on 21 February 2007. Based on this fog case, Hu et al. (2019) (hereafter referred to as Hu2019) investigated the sensitivity of fog forecasts to synoptic-scale initial errors by using composite analyses based on ensemble forecasts. Their results indicated that there were significant synoptic-scale initial differences between groups of good-performing and bad-performing ensemble members. Moreover, the evolution of these initial differences, which was consistent with the evolution of the main features of the CFSP, consequently caused the failure of fog forecasting for bad-performing members by adversely influencing temperature advection (the governing dynamic factor). It was therefore speculated that there may be synoptic-scale adaptive locations for sea fog forecasting. Based on the same case, results in Hu et al. (2014) (hereafter referred to as Hu2014) showed that improvement of fog forecasts due to the linear improvement of initial temperature advection (the governing dynamic factor) was gradual, which is significantly different from the strong nonlinear behavior documented by Zhang and Sippel (2009) in their study of a TC. This suggests that adaptive observations based on the ESA method may provide greater potential benefits for fog forecasting than for previously studied TC prediction (Xie et al., 2013). Additionally, results by Ancell and Hakim (2007) indicated that ensemble sensitivity fields emphasize synoptic-scale features. Therefore, this study focused on exploring the observation strategy and effectiveness of synoptic-scale adaptive locations for sea fog forecasting with the CFSP, and the ESA method, as applied in Xie et al. (2013), was adopted.

Three interesting questions were addressed in this study: (1) How should adaptive locations for fog forecasts be identified using the ESA method? In other words, what is the suitable target observation type and forecast metric for sea fog adaptive observations using this method? In previous adaptive observation studies, the observation type (such as dropsondes for TC prediction and soundings for ozone prediction) was preset, and they focused on determining adaptive locations for the preset observation type. Actually, the target observation type is the basis for identifying adaptive locations, so it is necessary to objectively select the target observation type before identifying adaptive locations. (2) Where do the adaptive locations occur, and how reasonable are the underlying physical conditions? (3) How effective are synoptic-scale adaptive observations for fog forecasts? From the perspective of predictability, these questions correspond to the most sensitive variables and regions in ICs, and how the key initial errors develop.

To answer these three questions, the 2007 fog event, which exhibited typical CFSP features, was selected as a case study. As this study is a preliminary attempt to explore the impact of adaptive observations on sea fog forecasts, it is important to first explore the true observation impact of the ESA method on fog forecasts. Similar to Xie et al. (2013), to avoid errors caused by observations and an imperfect model and investigate the true observation impact given by the algorithm, numerous observation system simulation experiments (OSSEs) were conducted by assimilating synthetic observations of the target observation type without adding observation errors and using the same forecast model with optimized model configurations. Furthermore, as the issue of most concern in practical targeting applications, the real effectiveness of adaptive observations under actual conditions was examined by conducting sensitivity experiments (hereafter referred to as REALs) by assimilating real observations of the target observation type at locations the same as used in OSSEs. Both OSSEs and REALs were performed in conjunction with the WRF model, which has been widely used for sea fog forecasting in both studies and operational applications (Gao et al., 2007; Wang et al., 2014). Previous researchers (Hamill and Snyder, 2002; Bei et al., 2012) have suggested that it is better to employ advanced data assimilation (DA) schemes to obtain consistently positive results for adaptive observations. Hence, the ensemble Kalman filter (EnKF) DA scheme within the WRF model, which was also used by Xie et al. (2013), was adopted in this study to investigate the effectiveness of adaptive observations. Moreover, to verify the conclusions obtained in the 2007 fog case, another typical sea fog event with CFSP characteristics was also studied. Note that in this study, we only focused on the surface fog coverage, which is defined as the area consisting of points with a surface liquid water content (LWC) higher than 0.016 g kg^{-1} (Gultepe et al., 2007). Given that the sea fog formation and maintenance suffered more forecast uncertainties than its dissipation for the 2007 fog case (Hu et al., 2014), which was possibly due to the more complex processes involved in fog formation and maintenance, this study focused on forecasts of fog formation and maintenance.

The rest of this paper is organized as follows: The ESA method is described in section 2. The main part for the case study is provided in section 3, including an overview of the case, design and configuration of the experiments, validation method for fog forecasting, and experimental results. Verification based on another sea fog case with CFSP characteristics is presented in section 4. In section 5, the impact of observation and model errors is discussed. Finally, a summary is

given in section 6.

2. ESA for adaptive observation purposes

In this study, the ESA method identifies the adaptive location that will maximize the decrease in the model uncertainty with the norm of change in the ensemble forecast-error variance of user-defined model state variables. The mathematical details of the ESA method have been reported in Bei et al. (2012) and Xie et al. (2013). Briefly, change in the forecast error variance can be expressed as

$$\mathbf{P}_\mathrm{b}-\mathbf{P}_\mathrm{a}=\mathbf{P}_\mathrm{b}\mathbf{H}^\mathrm{T}(\mathbf{H}\mathbf{P}_\mathrm{b}\mathbf{H}^\mathrm{T}+\mathbf{R})^{-1}\mathbf{H}\mathbf{P}_\mathrm{b}\,, \tag{1}$$

where $\mathbf{P}_\mathrm{b}$ and $\mathbf{P}_\mathrm{a}$ are the background and analysis error covariance matrices, respectively; $\mathbf{H}$ is a linear operator matrix that relates the model state variables to the observational variables; $\mathbf{H}^\mathrm{T}$ is the transpose of $\mathbf{H}$; and $\mathbf{R}$ is the observational error (the instrument and representation errors) covariance matrix.

In numerical weather prediction, as the true state is unknown, $\mathbf{P}_\mathrm{b}$ can be estimated using an ensemble covariance matrix around the ensemble mean, i.e., $\bar{\mathbf{x}}_\mathrm{b}=\frac{1}{N}\sum_{i=1}^{N}\mathbf{x}_{\mathrm{b},i}$, where $\mathbf{x}_\mathrm{b}$ is the model background state vector before DA. Hence, $\mathbf{P}_\mathrm{b}$ can be expressed as

$$\mathbf{P}_\mathrm{b}=\frac{1}{N-1}\sum_{i=1}^{N}(\mathbf{x}_{\mathrm{b},i}-\bar{\mathbf{x}}_\mathrm{b})(\mathbf{x}_{\mathrm{b},i}-\bar{\mathbf{x}}_\mathrm{b})^\mathrm{T}=\mathbf{X}_\mathrm{b}(\mathbf{X}_\mathrm{b})^\mathrm{T}\,, \tag{2}$$

where i and N are the ensemble member and total ensemble size, respectively. $\mathbf{X}_\mathrm{b}$ is a matrix of background ensemble perturbations, where each column is $(\mathbf{x}_{\mathrm{b},i}-\bar{\mathbf{x}}_\mathrm{b})$. Substituting Eq. (2) into Eq. (1) yields the following:

$$\mathbf{P}_\mathrm{b}-\mathbf{P}_\mathrm{a}=\mathbf{X}_\mathrm{b}(\mathbf{H}\mathbf{X}_\mathrm{b})^\mathrm{T}[\mathbf{H}\mathbf{X}_\mathrm{b}(\mathbf{H}\mathbf{X}_\mathrm{b})^\mathrm{T}+\mathbf{R}]^{-1}\mathbf{H}\mathbf{X}_\mathrm{b}(\mathbf{X}_\mathrm{b})^\mathrm{T}\,. \tag{3}$$

Then, to obtain the ensemble forecast-error variance, forecasts obtained from ICs with and without the assimilation of additional observations are compared. If these two forecasts are denoted by the superscripts f|a and f|b, respectively, the change in the forecast error variance is the trace of $\mathbf{P}_\mathrm{f|a}-\mathbf{P}_\mathrm{f|b}$. When the analysis errors are small, the reduction in the forecast error variance can be estimated as (Bishop et al., 2001; Majumdar et al., 2001)

$$\begin{aligned}\mathbf{P}_\mathrm{f|b}-\mathbf{P}_\mathrm{f|a}&\approx\mathbf{M}(\mathbf{P}_\mathrm{b}-\mathbf{P}_\mathrm{a})\mathbf{M}^\mathrm{T}\\&\approx\mathbf{M}\mathbf{X}_\mathrm{b}(\mathbf{H}\mathbf{X}_\mathrm{b})^\mathrm{T}[\mathbf{H}\mathbf{X}_\mathrm{b}(\mathbf{H}\mathbf{X}_\mathrm{b})^\mathrm{T}+\mathbf{R}]^{-1}\mathbf{H}\mathbf{X}_\mathrm{b}(\mathbf{M}\mathbf{X}_\mathrm{b})^\mathrm{T}\,,\end{aligned} \tag{4}$$

where $\mathbf{M}$ is the linear model forecast operator, and $\mathbf{M}^\mathrm{T}$ is its transpose. Similar to considering the ensemble forecast from the ensemble background, we can obtain $\mathbf{X}_\mathrm{f|b}=\mathbf{M}(\mathbf{X}_\mathrm{b})$. Then, if $\mathbf{H}\mathbf{X}_\mathrm{b}$ can be replaced by $\mathbf{Y}$, which represents the observations located at the model grid points, Eq. (4) can be rewritten as

$$\mathbf{P}_\mathrm{f|b}-\mathbf{P}_\mathrm{f|a}\approx\mathbf{X}_\mathrm{f|b}\mathbf{Y}^\mathrm{T}\left[\mathbf{Y}\mathbf{Y}^\mathrm{T}+\mathbf{R}\right]^{-1}\mathbf{Y}(\mathbf{X}_\mathrm{f|b})^\mathrm{T}\,, \tag{5}$$

where $\mathbf{X}_\mathrm{f|b}$ is the user-defined forecast metric, $\mathbf{Y}$ is selected as a vector of observations located at model grid points of the background state, and $\mathbf{R}$ denotes the observation error variance of the selected observed variables, with values consistent with those at rawinsonde locations provided by the WRF variational DA system (Parrish and Derber, 1992).

Based on Eq. (5), $\mathbf{P}_\mathrm{f|b}-\mathbf{P}_\mathrm{f|a}$ can be approximated for each candidate observation location (model grid point). We defined the impact factor as the trace of $\mathbf{P}_\mathrm{f|b}-\mathbf{P}_\mathrm{f|a}$ at the respective time (Stuart et al., 2007). Locations with the maximum impact factor values were expected to produce the greatest reduction in uncertainty for the defined forecast metric and were therefore selected for additional adaptive observations.

Given that this study focuses on the simulation of fog coverage, the concept of fog points, which are points with the LWC exceeding 0.016 g kg^{-1}, is used for defining the forecast metric. Accordingly, the forecast metric used in this study is defined as the area-averaged fog point ratio (FPR)—namely, the ratio of fog points to the total grid/observed points, in the verification region (see section 3.4.1). Results of tests with using different forecast metrics to identify adaptive locations showed that the identified sensitive area with FPR as the forecast metric is more physically reasonable than other forecast metrics used in previous studies, such as the total energy norm (Zhang et al., 2016).

Two observation vectors are used in this study: the selected specific variable at a specific pressure level at each model grid point to identify the target observation type, and the identified target observation type at each model grid point to identify the adaptive locations. For the first observation vector, given that initial data on the temperature, humidity, and horizontal wind are all important for fog formation and maintenance (Zhou and Ferrier, 2008; Zhou, 2011), and considering the observed variables and vertical levels in the real observation types (i.e., rawinsondes, wind profilers, and automatic weather stations), we selected four meteorological observational variables (temperature, dewpoint temperature, and zonal and meridional winds) and twelve typical pressure levels (surface, 1000, 925, 850, 700, 500, 400, 300, 200, 150, and 100 hPa). Then, the expected (predicted) observation impact (impact factor) of different selected variables at different pressure levels on the FPR were calculated individually using Eq. (5) for comparison to define the target observation type. The vertical distribution of the impact factor could be obtained by calculating the horizontally averaged impact factor over all grid points, and the horizontal distribution of the impact factor could be obtained by calculating the impact factor at each specific pressure level at each grid point. The target observation type was defined as a composite of the observed variables and pressure levels that exhibit dominant observation impacts. For the second type of observation vector, the horizontal distribution of the impact factor could be obtained by calculating the sum of the impact factor at all pressure levels of the target observation type. Adaptive loca-

tions were defined as isolated regions with greater observation impacts that developed both in magnitude and extent until the verification time.

3. Study of the 2007 fog case

3.1. *Case overview*

A detailed case overview (dots in Figs. 1a–d and shading in Fig. 1e) of the 2007 fog case is provided in Hu2014. At 1200 UTC (2000 LST) 20 February 2007, fog (red dots) was observed only at the southern tip of Liaoning Province. Twelve hours later (0000 UTC 21 February), fog was observed in the majority of the coastal regions around the Bohai Sea. At 0300 UTC 21 February, although fog at some tips of the coastal regions dissipated due to local sunrise, the main part of the sea fog coverage area was maintained, and this fog event reached a mature stage. Due to the intrusion of cold air from the northeast at 2000 UTC 21 February 2007, fog began to dissipate (figures not shown). This fog event lasted more than 24 h and severely impacted local transportation but was poorly predicted by operational and research weather prediction systems. Given that this study investigated forecasts of fog formation and maintenance, we focused on the period between 1200 UTC 20 February 2007 (actual fog formation) and 0300 UTC 21 February 2007 (actual fog maintenance).

As documented in Hu2019, the main features of this synoptic pattern were a dominant high-level ridge behind the trough associated with the cold front and a surface high over the sea along the southeast direction after cold-front passage. Specifically, the upper-level circulation moved eastward following a trough–ridge–trough form, and the region of interest was dominated by the ridge. Closer to the surface, passage of the cold front over the region of interest pushed the surface high to the southeast over the sea (schematic in Fig. 2). Under this synoptic pattern, synoptic conditions conducive to fog formation tend to occur—namely, a cold local surface after cold-front passage, abundant warm moist backflow from the surface high, and stable high-level conditions generated by the dominant ridge.

3.2. *Design and configuration of the experiments*

A flowchart of the experimental design for this case is depicted in Fig. 3.

First, a 40-member ensemble (hereafter referred to as EN40_FNL; see section 3.2.1) was obtained with the initial ensemble generated by perturbing the NCEP FNL data with a horizontal resolution of 1° × 1° at the original initial time. Based on EN40_FNL, two members with a relatively poor performance and the best performance in approximating the observed fog coverage evolution were selected and renamed the NoDA (no assimilation, control) and TRUE runs, respectively.

Then, to determine the target observation type and corresponding adaptive locations with the ESA method, a new

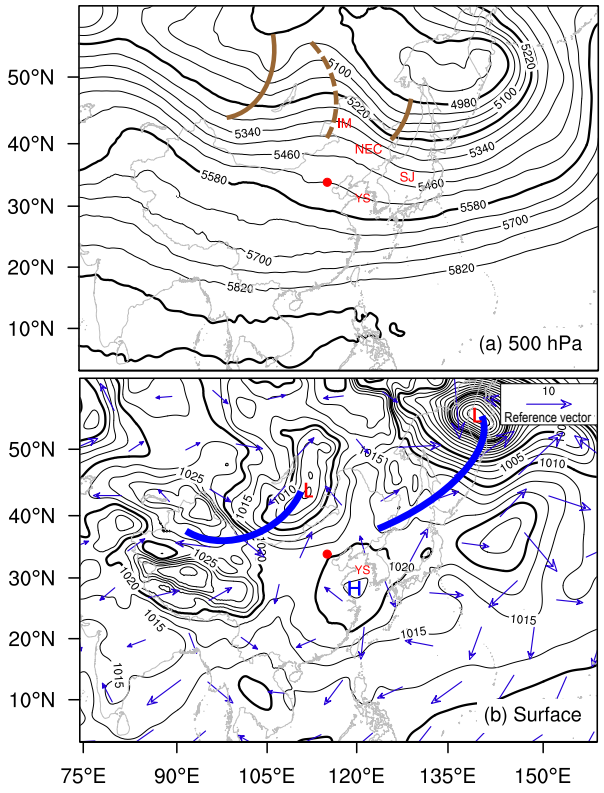

Fig. 2. Schematic [cited from Fig. 2 of Hu et al. (2019)] of the CFSP: synoptic chart at (a) 500 hPa and (b) the surface at 1800 UTC 20 February 2007 (before the actual fog formation). The brown solid and dashed lines in (a) represent the trough and ridge lines, respectively. The thick blue lines in (b) represent the location of the cold front. The blue vectors in (b) represent the 10-m horizontal wind. Abbreviations: IM, Inner Mongolia; NEC, Northeast China; SJ, Sea of Japan. This figure is based on United States National Centers for Environmental Prediction (NCEP) Final Analysis (FNL) data.

ensemble forecast (hereafter referred to as EN40_POOR) was generated by perturbing the ICs of the NoDA run with the same initialization method as used for EN40_FNL.

Next, as mentioned in the Introduction, to assess the true observation impact given by the ESA method and the actual observation impact for fog forecasts, OSSEs and REALs were conducted by assimilating individual synthetic and real observations, respectively, at the target time followed by a period of WRF simulation. The first guess for all assimilation experiments was obtained from the forecast field of NoDA at the target time. The synthetic observations for OSSEs were obtained based on the TRUE run (see section 3.2.2).

3.2.1. *Generation of EN40_FNL and EN40_POOR*

The Advanced Research version of the WRF model, version 3.3.1 (Skamarock et al., 2008), was used in this study for fog forecasts. The model configuration and physical parameterization schemes, the same as those adopted in Hu2014 and Hu2019, have been tuned to obtain optimized configurations for sea fog forecasts of this case. Three

domains (Fig. 4) with horizontal grid spacings of 27 km (D1), 9 km (D2), and 3 km (D3) were applied with two-way nesting. There were 40 full sigma levels, with the vertical resolution below 1 km increased (the heights were approximately

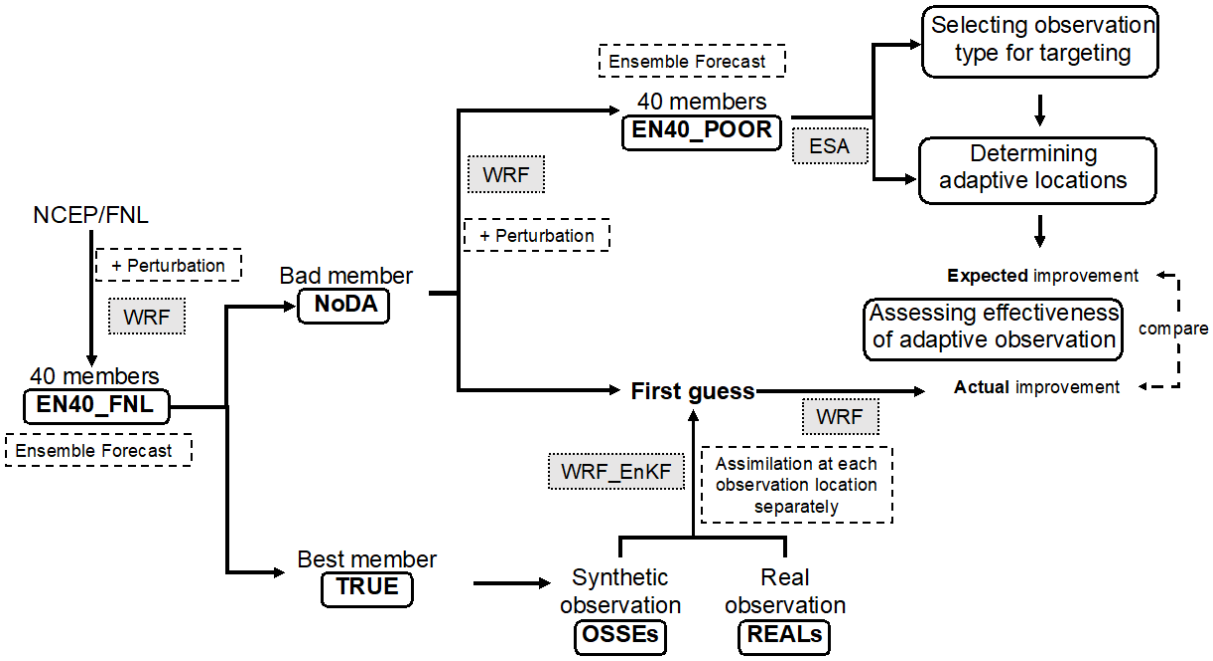

Fig. 3. Flowchart of the experimental design for the 2007 fog case.

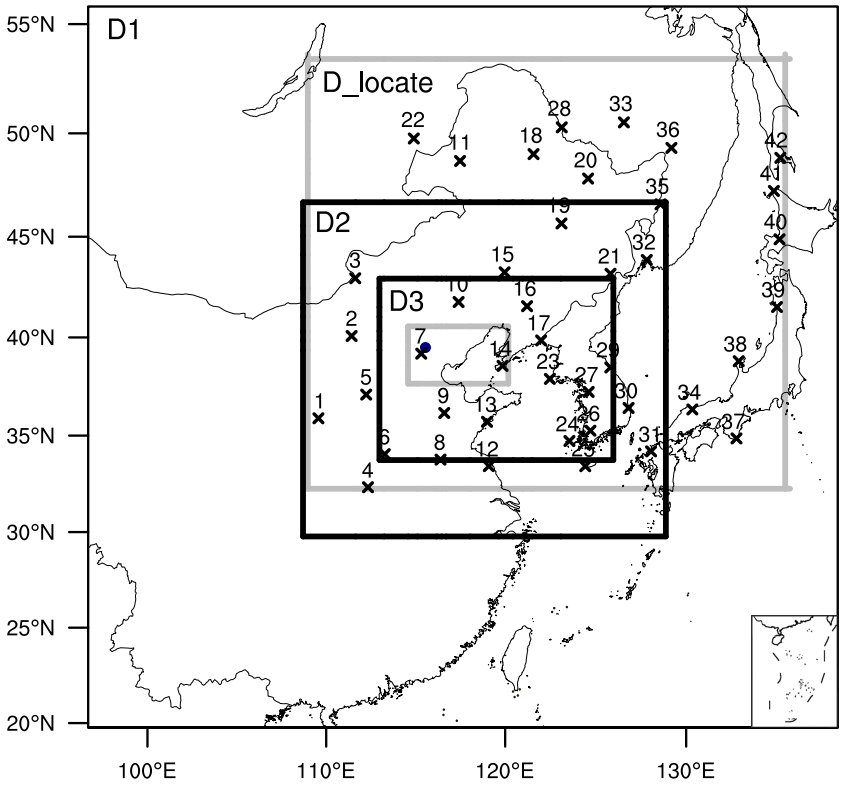

Fig. 4. Nested configuration of the model domains. Black boxes denote the model domains (D1, D2, and D3). The outer large gray box denotes the region used to locate different single synthetic/real observations for examining the effectiveness of adaptive observation (D_locate, same box in Fig. 9b). The inner small gray box denotes the selected verification region. Black crosses within D_locate denote the locations of synthetic/real observations for DA in the OSSEs/REALs. The navy blue dot in the inner gray box denotes the location of Beijing

27, 94, 184, 299, 444, 630, and 859 m), and the model top at 50 hPa. The WRF single-moment 6-class microphysics scheme (Hong and Lim, 2006), Rapid Radiative Transfer Model longwave radiation scheme (Mlawer et al., 1997), Dudhia shortwave radiation scheme (Dudhia, 1989), and quasi-normal scale elimination PBL and surface layer schemes (Sukoriansky et al., 2005) were used for all three domains. The Kain–Fritsch cumulus scheme (Kain, 2004) was used only for D1 and D2. Compared to the conventional 30-s United States Geological Survey land-use data (Hitt, 1994), the WRF simulations used more realistic vegetation information for D3, which was based on 500-m resolution land-use data for the year 2000 (Zhang et al., 2007). To be consistent with our previous work on this fog case, i.e., Hu2014 and Hu2019, sea surface temperature (SST) information used in this study was from FNL data rather than from data with finer resolution, such as the North-East Asian Regional-Global Ocean Observing System (NEAR-GOOS) daily SST data. Actually, there were no obvious differences in the fog forecast results obtained between sensitivity experiments based on the FNL SST data and NEAR-GOOS daily SST data for this case.

The ensemble initialization method for EN40_FNL was the same as adopted in previous studies (Hu et al., 2014; Huang and Meng, 2014), in which the ICs of the ensemble forecasts were generated by randomly perturbing the FNL data at 0000 UTC 20 February 2007 (0800 LST, the original initial time). The perturbations were obtained by randomly sampling the background error covariance from the WRF-3DVar fixed-covariance model (Skamarock et al., 2008). The standard deviations of the initial ensemble were roughly 1.2 K for air temperature, 3 m s^{-1} for wind, and 0.3 g kg^{-1} for the water vapor mixing ratio. The whole ensemble was then integrated for 27 h. Except for the ICs, all 40 members used the same model configuration, physical parameterization schemes, and boundary conditions obtained from 6-h FNL data.

EN40_POOR was also integrated for 27 h, with the first 12-h integration of the ensemble forecast used to develop an approximately realistic flow-dependent background error covariance structure (Zhang, 2005; Yue and Meng, 2017) for calculating observation impacts and conducting assimilation.

3.2.2. *OSSE and REAL configurations*

Observations used for assimilation in this study were synthetic and real observations of the target observation type—namely, temperature at 850 hPa and the surface layer (hereinafter referred to as 850hPa-and-surface temperature; see section 3.4.2). Because field experiments of adaptive observation for sea fog forecasts have not yet been conducted, the real 850hPa-and-surface temperature data used in this study are actually the real observed temperature information at 850 hPa and the surface extracted from real radiosonde observations. This treatment can be considered reasonable because these alternative real observations have included important factors for actual conditions (i.e., observation errors), and the real locations of these observations could represent different adaptive/nonadaptive locations for assessing the effectiveness of adaptive observations. Given that radiosonde observations at different locations have been separately used to obtain single real 850hPa-and-surface temperature observations rather than being assimilated as a whole, to be fair, other existing observations, such as conventional surface and sounding observations and satellite data, have not been assimilated in this study.

For the OSSEs, synthetic 850hPa-and-surface temperature observations were generated by extracting temperature information from the TRUE run at 1200 UTC 20 February 2007 (the target time) without adding observation errors. Note that because this study focused on synoptic-scale adaptive observations, the TRUE run in the coarsest domain (D1) was used for generating synthetic observations, and only the model field in D1 was updated through DA with the increments (posterior minus prior) in assimilating observations in D1 projected to D2 and D3. Thus, to compare the observational impacts of the observations at different locations on fog forecasts, 42 synthetic 850hPa-and-surface temperature observations with locations according to real radiosonde data (black crosses in Fig. 4) within the region of D_locate (outer gray box in Fig. 4, see section 3.4.4) were derived from the TRUE run in D1. Then, a set of analyses was generated by individually assimilating each of the 42 synthetic 850hPa-and-surface temperature observations at the assimilation time (same as the target time in this study) with the WRF-EnKF model. Accordingly, 42 separate deterministic forecasts were initialized with the corresponding EnKF mean analyses and integrated for 15 h. Note that to ensure the EnKF and ESA methods use consistent ensemble statistics, following the treatment used in Xie et al. (2013), we did not apply localization for the WRF-EnKF model in this study. In addition, this study only focuses on the performance of deterministic forecasts based on the EnKF mean for each assimilation–forecast experiment. The ensemble forecast performance for each assimilation–forecast experiment was not investigated in this study due to the limitations in computing resources. The NoDA run is also the deterministic forecast with ICs retrieved from the ensemble mean of EN40_POOR in the following sections.

For the REALs, the experimental design is the same as that of the OSSEs except that the observations assimilated were real observations instead of synthetic observations.

3.3. *Validation method for fog forecasting*

Because this study focused on surface fog coverage, which is defined based on the point-to-point LWC, the fog forecast performance was evaluated through the simulated fog coverage, which was correspondingly defined as the area consisting of points with a simulated LWC at the first model vertical level (hereinafter referred to as lev1) in D3 higher than 0.016 g kg^{-1}. Note that although low clouds are frequent during coastal sea fog, only grounded clouds (fog) were the focus of this study. Hence, the simulated LWC at lev1, instead of at multiple vertical levels, was used for defin-

ing the simulated fog coverage. To quantitatively evaluate the fog forecast performance, the threat score (TS), false alarm ratio (FAR), and missing ratio (MR) were used as measures of prediction accuracy. As documented in Hu2019, considering fog observations/forecasts as binary events (1 = true, 0 = false), the predictive skill scores can be calculated as follows:

$$\mathrm{TS} = \frac{A_c}{A_f + A_o - A_c}, \tag{6}$$

$$\mathrm{FAR} = \frac{A_f - A_c}{A_f}, \tag{7}$$

and

$$\mathrm{MR} = \frac{A_o - A_c}{A_o}, \tag{8}$$

where A_f, A_o, and A_c denote the fog forecasts, fog observations, and correct (hit) fog forecasts, respectively. Larger TS values (smaller FAR and MR values) indicate a better forecast performance.

To validate the ensemble forecasts (EN40_FNL and EN40_POOR), similar to the validation method documented in Hu2019, the forecast performance of each member was objectively evaluated through comprehensive consideration of the predictive skill scores (TS, FAR, and MR) calculated against station data from a temporal perspective and against satellite data from a spatial perspective. The ensemble members with a better forecast performance were those that exhibited larger TS values and smaller FAR and MR values. From a temporal perspective, the simulated LWC values at lev1 at each observation station (dots in Figs. 1a–d) were compared to the corresponding observed surface-observed visibility every 3 h from 1200 UTC 20 February 2007 to 0300 UTC 21 February 2007—namely, the stage of actual fog formation and maintenance. Here, LWC $\geq$ 0.016 g kg^{-1} corresponded to visibility $\leq$ 1 km. From a spatial perspective, the simulated LWC values at lev1 at each point in D3 (Fig. 1e) were compared to the corresponding observed fog points derived from MTSAT data, with the same detection method as that used in Wang et al. (2014), at 0300 UTC 21 February 2007 (actual fog mature stage).

In the case of the assimilation–forecast experiments (OSSEs and REALs), given that the time of 0300 UTC 21 February 2007 was specified as the verification time of adaptive observation (see section 3.4.1), the results of the OSSEs and REALs were evaluated only at this time from a spatial perspective. Thus, the TRUE run and satellite data were used as the references for the OSSEs and REALs, respectively, and the predictive skill scores were calculated from a spatial perspective. In other words, to calculate the predictive skill scores for the OSSEs, the satellite data were replaced by the simulated LWC at lev1 at 0300 UTC 21 February 2007 obtained from the TRUE run. Moreover, to emphasize the benefits of assimilating observations for the fog forecast performance, the improvements ("$\mathrm{I_{mprov}}$") in the predictive skill scores were defined as follows:

$$\mathrm{I_{mprov}\ TS} = \mathrm{TS(OSSEs/REALs)} - \mathrm{TS(NoDA)}, \tag{9}$$

$$\mathrm{I_{mprov}\ FAR} = \mathrm{FAR(NoDA)} - \mathrm{FAR(OSSEs/REALs)}, \tag{10}$$

and

$$\mathrm{I_{mprov}\ MR} = \mathrm{MR(NoDA)} - \mathrm{MR(OSSEs/REALs)}. \tag{11}$$

3.4. *Results*

3.4.1. *TRUE, NoDA, and EN40_POOR runs*

Based on the temporally and spatially averaged predictive skill scores and evolution of the simulated fog coverage for each ensemble member in EN40_FNL, member_10 and member_38 exhibited the best performance and a very poor performance, respectively, among the 40 ensemble members. The predictive skill scores for these two members and the mean of the 40 members are shown in Figs. 5a–c. Compared to the observations (dots in Figs. 1a–d and shading in Fig. 1e), both runs captured the main fog formation process in Shandong Province. However, in the main part of the Bohai Sea and its coastal region (the area is shown in the blue rectangular box in Figs. 5g and k, and the inner gray box in Fig. 4), member_10 (shading in Figs. 5d–g) simulated the fog process with a close resemblance to the observations, while member_38 (shading in Figs. 5h–k) missed the fog coverage entirely in the focal regions. Thus, member_10 and member_38 were selected as good and bad members and correspondingly regarded as the TRUE run and NoDA runs, respectively. The region indicated by the blue rectangular box in Figs. 5g and k, which suffers vulnerability of heavy transportation to sea fog and high fog forecast uncertainties, was specified as the verification region for this case.

Figure 6 shows the spread of simulated fog coverage produced from ENS40_POOR. Similar to the forecast from the ensemble mean, most members failed to capture the main fog formation process in the verification region, with lower TS and higher FAR and MR values than that of the TRUE run. Additionally, the ensemble forecast exhibited a large discrepancy of the simulated fog coverage in the verification region, especially at 0300 UTC 21 February 2007 (the end of simulation). This implies the rationality of the ensemble forecast, which has reasonable initial ensemble spread (figures not shown). Hu2014 indicated that this large forecast discrepancy is closely related to the significant differences in ICs between the TRUE run and NoDA run. Thus, the high initial uncertainties provided the motivation to investigate adaptive observations as a means to improve sea fog forecasting in this case.

Given that there were high uncertainties in the fog coverage forecast at 0300 UTC 21 February 2007, and based on our previous study in which we found that the results from

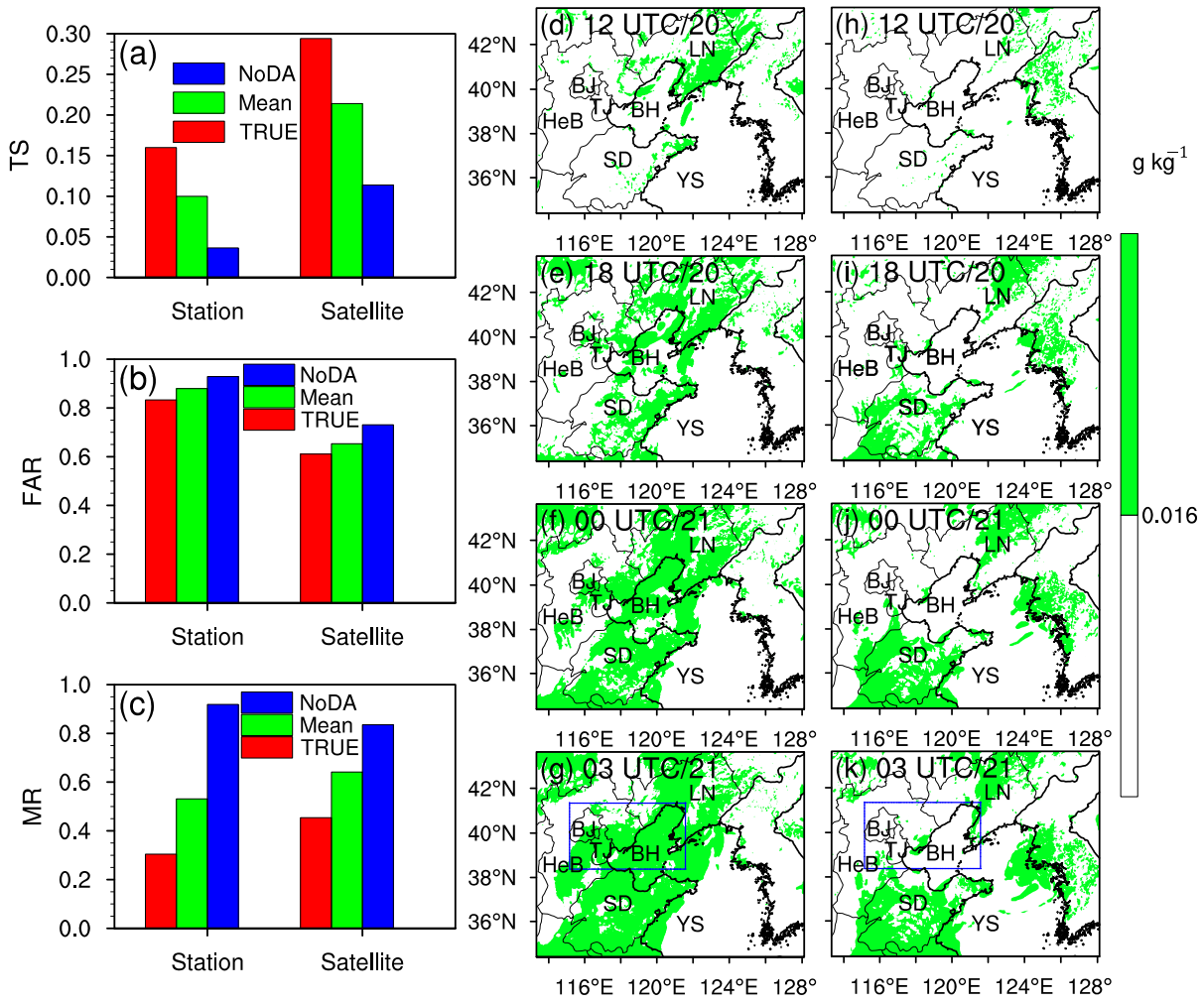

Fig. 5. (a–c) Temporally averaged (marked "Station") and spatially averaged (marked "Satellite") (a) TS, (b) FAR, and (c) MR, for the TRUE run (red), NoDA run (blue), and mean of ENS40_FNL (green). (d–k) Simulated fog coverage (shading), defined as the area of points with simulated LWC ⩾ 0.016 g kg^{-1} at the first model vertical level in the innermost model domain, for the (d–g) TRUE run and (h–k) NoDA run, at 1200 UTC and 1800 UTC 20 February 2007, and 0000 UTC and 0300 UTC 21 February 2007, respectively. The blue rectangular box in (g) and (k) is chosen as the verification region for forecast metrics to be examined.

evaluating the sea fog forecast performance from the temporal aspect (the stage of actual fog formation and maintenance) and from the spatial aspect (at 0300 UTC 21 February, the actual fog mature stage) were similar, the time of 0300 UTC 21 February 2007 was specified as the verification time for adaptive observation for this case.

3.4.2. *Defined observation type for targeting*

First, to outline the general characteristics of observation impacts of different variables at different pressure levels, the vertical distributions of the expected observation impacts of the four selected observed variables (Fig. 7) were compared. Generally, for each of the four selected variables, the expected observation impact below 700 hPa was larger than that at the other pressure levels. Additionally, the expected observation impact of the temperature was much larger than that of the other variables at the corresponding pressure levels, especially with a peak at 850 hPa. These results agree with the results of Hu2014 indicating that the initial errors of the low-level temperature impose a larger adverse influence on fog forecasts than those of humidity and horizontal winds. Therefore, temperatures below 700 hPa were preliminarily selected as the target observation type in this case.

Furthermore, given that both the concentration (relatively localized and compact) and growth (magnitude and extent) of regions with large expected observation impacts are significant when identifying the target observation type and the corresponding adaptive locations, we analyzed the evolution of the spatial distribution of the expected observation impact of the temperature at the different pressure levels, especially temperatures below 700 hPa (Fig. 8). The region of a large expected observation impact of the temperature below 850 hPa (Figs. 8b–e) is consistently concentrated with respect to the pattern and location, and develops both in magnitude and extent; in contrast, the region of a large

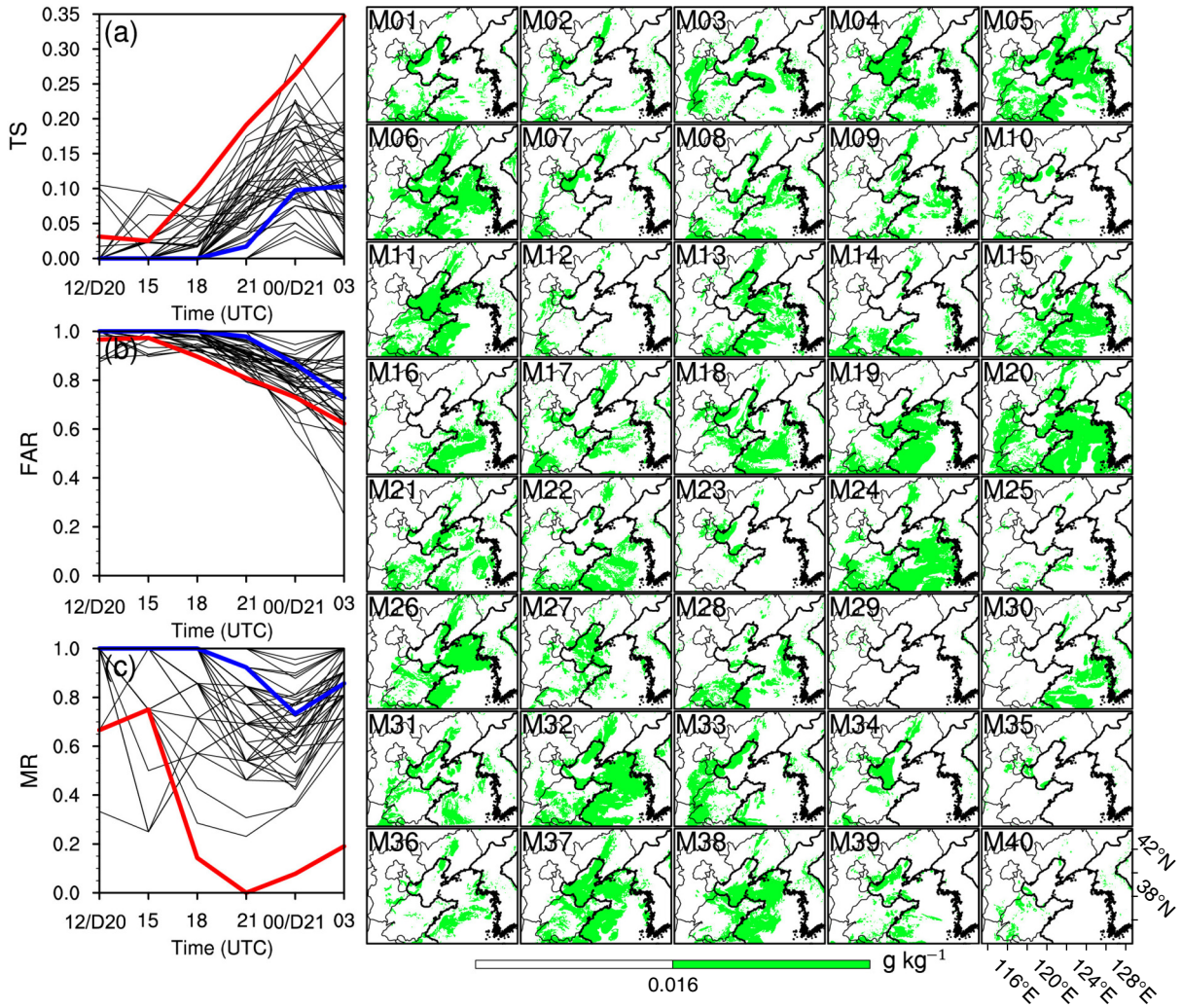

Fig. 6. (a–c) Evolution of area-averaged TS, FAR, and MR for the TRUE run (red), NoDA run (blue), and EN40_POOR (black) in the verification region evaluated based on surface station observations. 12/D20 and 00/D21on the *x*-axis represents time at 1200 UTC 20 and 0000 UTC 21, respectively. Right: same as Figs. 5d–k, but for simulated fog coverage from EN40_POOR at 0300 UTC 21 February 2007.

expected observation impact at 700 hPa (Fig. 8a) at 0600 UTC 20 February is inconsistent with the corresponding pattern and location at 850 hPa and below and gradually decreases. Therefore, temperature at 700 hPa was excluded from the selection of the target observation type. Moreover, given that the expected observation impact in most areas within D1 at 925 hPa and 1000 hPa cannot be calculated due to the local topography (the blank area within D1 in Figs. 8c and d), to ensure a more reasonable calculation of the impact factor, 850 hPa and the surface were selected to represent the situation of the temperature at a low level in this study. Actually, this selection is reasonable because temperature information at 850 hPa and the surface can represent the impact of the low-level vertical thermal structure (from the combination of the 850-hPa- and surface-layer temperatures) and underlying surface (from the surface layer) on fog forecasts.

Therefore, the temperature at 850 hPa and the surface layer was defined as the 850hPa-and-surface temperature and was selected as the target observation type in this study. Note that although this study only focused on the potential observation impact of those four meteorological variables, further work is needed to explore the observation impact of SST and satellite-derived products including relative humidity because these parameters also play a potentially significant role in sea fog forecasts (Bari et al., 2015; Yang et al., 2021).

3.4.3. *Diagnosed observation impacts*

Figure 9 shows the expected impact factor for the individual 850hPa-and-surface temperature observations at 0600, 1200, and 1800 UTC 20 February 2007, with respect to the forecast of the FPR at the verification time. At 0600 UTC, 850hPa-and-surface temperature observations with relatively large observation impacts on the FPR metric (defined adaptive locations) were concentrated in the transition region between the surface low–high system. Six hours later (1200 UTC; target time), the area with a relatively large obser-

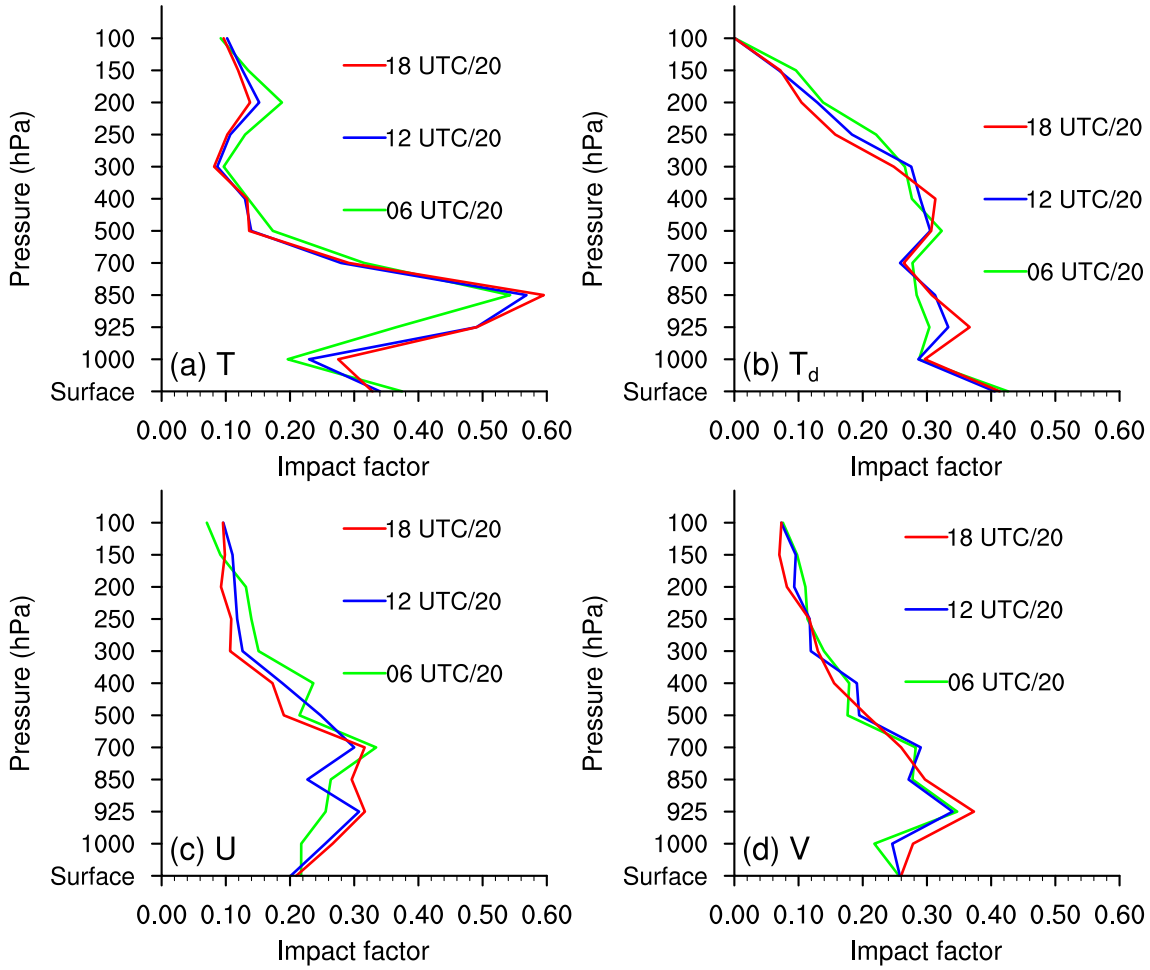

Fig. 7. Vertical distributions of the domain-averaged impact factor (units: 10^{-2}) of (a) temperature (T), (b) dewpoint temperature (T_d), and horizontal (c) zonal (U) and (d) meridional (V) wind in D1 at 0600 UTC (green), 1200 UTC (blue), and 1800 UTC (red) 20 February 2007, respectively. The impact factor was calculated with the FPR at the verification time in the verification region as the forecast metric and different variables (T, T_d, U and V) at different pressure levels as observations.

vation impact extended southward, which is consistent with the southerly extension of the surface low, and moved eastward, which agrees with the generally southerly movement of surface low–high systems. At 1800 UTC, the magnitude of the expected observation impacts continued to increase, and the area with relatively large observation impacts extended southward to the coastal region of the Bohai Sea. In general, the evolution of the area with a relatively large expected impact factor agreed well with the main features of the CFSP, as documented in section 3.1. This suggests that the identified adaptive locations were physically reasonable. Because 1200 UTC 20 February yields a clear local maximum of the impact factors and real observations are available at this time to verify the effectiveness of adaptive observations for fog forecasts, 1200 UTC 20 February was selected as the target time in this case.

3.4.4. *Actual improvement resulting from adaptive observations*

Given that the ESA method is based on a linear assumption that links the response of a given forecast metric to changes in ICs, it is necessary to verify the effectiveness of adaptive observations by statistically quantifying the relationship between the predicted observation impact and the actual changes in the forecast errors obtained from model integration through the assimilation of additional observations at different synthetic/real observation locations. In this study, the predicted and actual reductions in the root-mean-square error (RMSE) of the forecast metric were used as indicators to verify the effectiveness of adaptive observations, as used by Bei et al. (2012) and Xie et al. (2013). The predicted (expected) RMSE reduction in the forecast metric—namely, the FPR in the verification region at the verification time—was obtained by calculating the square root of the impact factor. To perform the comparison, the actual reduction in the RMSE was calculated from a comparison of the forecasts initialized from mean EnKF analysis of each OSSE/REAL and from NoDA.

To ensure the fairness of comparing the expected and actual observation impacts on the fog forecasts at the different

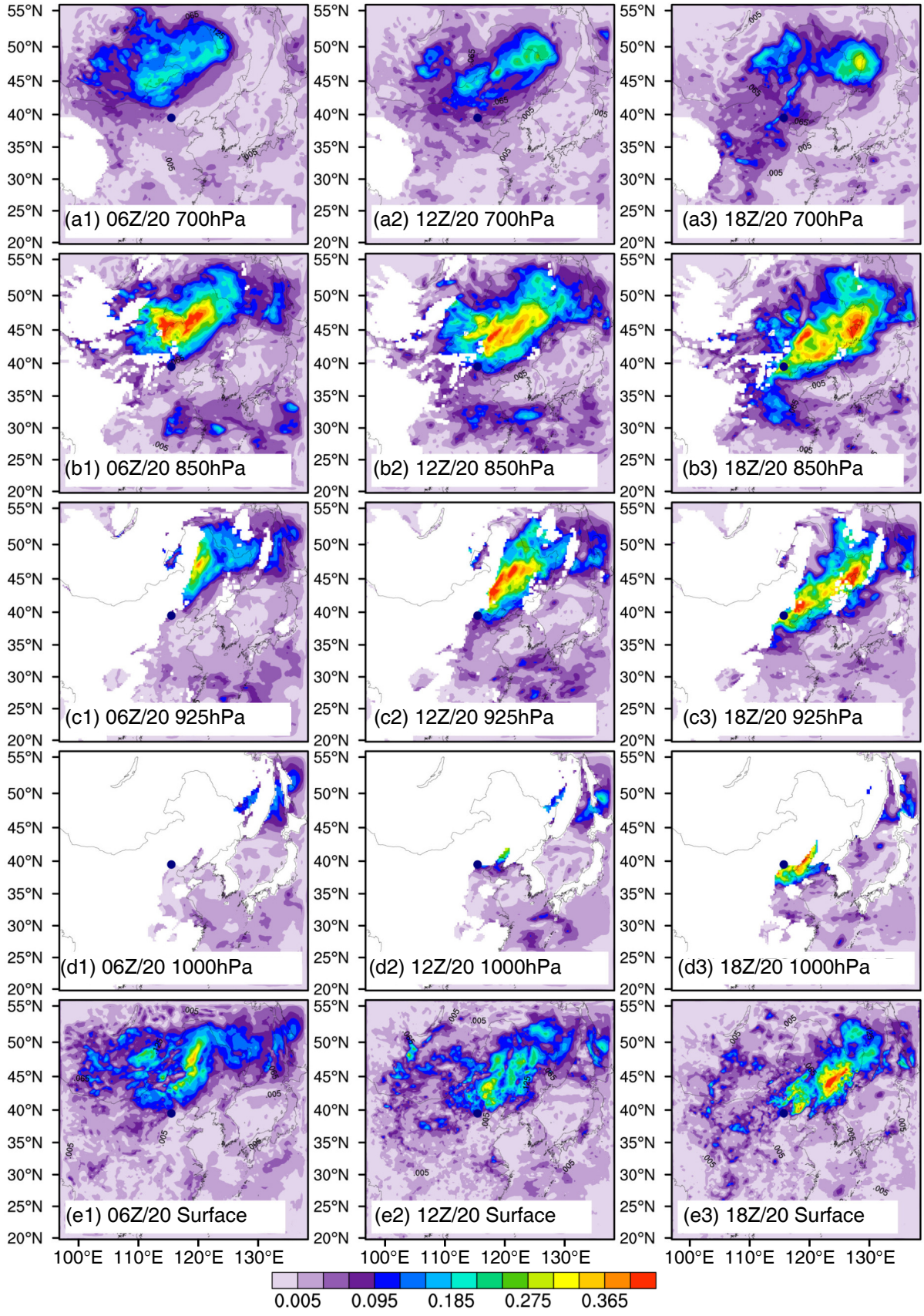

Fig. 8. Spatial distributions of the impact factor (units: 10^{-2}) of temperature at (a) 700 hPa, (b) 850 hPa, (c) 925 hPa, (d) 1000 hPa, and (e) the surface, in D1 at 0600 UTC (left column), 1200 UTC (middle column), and 1800 UTC (right column) on 20 February 2007, respectively. Calculation of the impact factor is the same as in Fig. 7.

locations and save computing resources, we fixed the region, as shown by the large box in Fig. 9b (hereinafter referred to as D_locate; namely, the outer gray box in Fig. 4), which contains both a subregion with relatively large expected observation impacts and a subregion with relatively small expected observation impacts at the target time. Additionally, the numbers of observation locations (the black crosses in Fig. 4) in those two subregions are similar.

3.4.4.1. OSSEs

The scatterplot and distribution of the expected and actual reductions in the RMSE of the FPR at the verification time for OSSEs are shown in Fig. 10a and Figs. 10c and d, respectively. In general, assimilating synthetic 850hPa-and-surface temperature in areas with larger predicted impact factors (larger expected reduction in the RMSE of the FPR), on average, resulted in a better sea fog forecast performance (larger actual reduction in the uncertainty in the FPR forecast) than assimilating temperature in areas with smaller predicted impact factors. Quantitatively, the correlation between the expected and actual reductions in the RMSE of the FPR could reach 0.643 and was significant at the 90% level of the *t*-test. This correlation value is much higher than that of the adaptive observations for TC prediction [0.38 for the RMSE of rainfall and 0.42 for the RMSE of the sea level pressure in Xie et al. (2013) without observation errors and under the perfect-model assumption] when the same ESA method was used. This suggests that the ESA method performs better for fog forecasts under this synoptic-scale pattern than for TC prediction, which verifies the hypothesis in the Introduction. For this better result for fog forecasts, one possible reason is that the strength of nonlinearity for the governing dynamics for TC prediction is much stronger than that of fog forecasts. Another possible reason is that the forecast metric used in this study is related to a larger-scale feature compared to the smaller features that were used in previous work on TC prediction.

Notably, it is interesting that the region of a large actual reduction in the RSME of the FPR (Fig. 10d) is concentrated in the transition region of the surface low–high system, which could be considered as the true adaptive locations based on the ESA method for fog forecasts in this case. This further indicates that a small position difference is most likely to create large RMSEs in the high-gradient region, so it is best to conduct observations there.

However, it should also be noted that the relative order of the actual reduction in the RMSE of the FPR at different observation locations does not agree well with the relative order of the corresponding expected values. For example, O10 exhibits the largest expected reduction in the RMSE of the FPR, while the observation location with the largest actual value is O20. This indicates that the true effectiveness of adaptive observations for fog forecasts given by the ESA method is limited. One possible reason is that, as mentioned by Bei et al. (2012), the actual error reduction through EnKF assimilation of synthetic 850hPa-and-surface temperature also depends on the magnitude of the differences between the observations and the model field (before assimilation), while the expected impact factor may not. Another possible reason is that the background error covariances for the EnKF method may be imperfect due to the limited ensemble size. Both are out of the scope of this study.

Additionally, in the experiments with the assimilation of observations at some locations with similar expected reductions in the RMSE, the corresponding actual reductions significantly differed. For example, when assimilating the 850hPa-and-surface temperature at the single locations of O18 and O42, the expected reductions in the RMSE of the FPR are similar, all approximately 0.045, while the actual reduction in the RMSE of the FPR for assimilating the observation at the location of O18 is much larger than that at the location of O42, which agrees with the results of the simulated fog coverage (Figs. 11a6 and a5) and the corresponding improvement in the predictive skill scores (Figs. 12a1–c1). This possibly occurs because compared to the location of O42, the location of O18 is much closer to the diagnosed adaptive locations (namely, the transition region of the surface low–high system) and is located upstream of the defined adaptive loca-

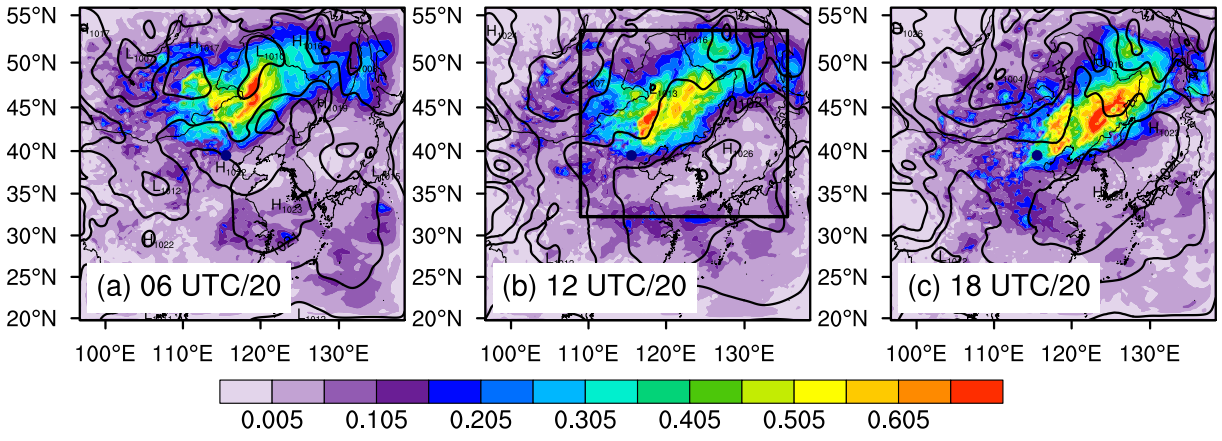

Fig. 9. Sea level pressure (contour lines) for the TRUE run, and the impact factor (shaded; units: 10^{-2}) of the FPR at the verification time in the verification region to 850hPa-and-surface temperature observations in D1 at (a) 0600 UTC, (b) 1200 UTC, and (c) 1800 UTC 20 February 2007, respectively. The large rectangular box in (b) denotes the region of D_locate, the same as the outer gray box in Fig. 4. The navy blue dot in each subplot denotes the location of Beijing.

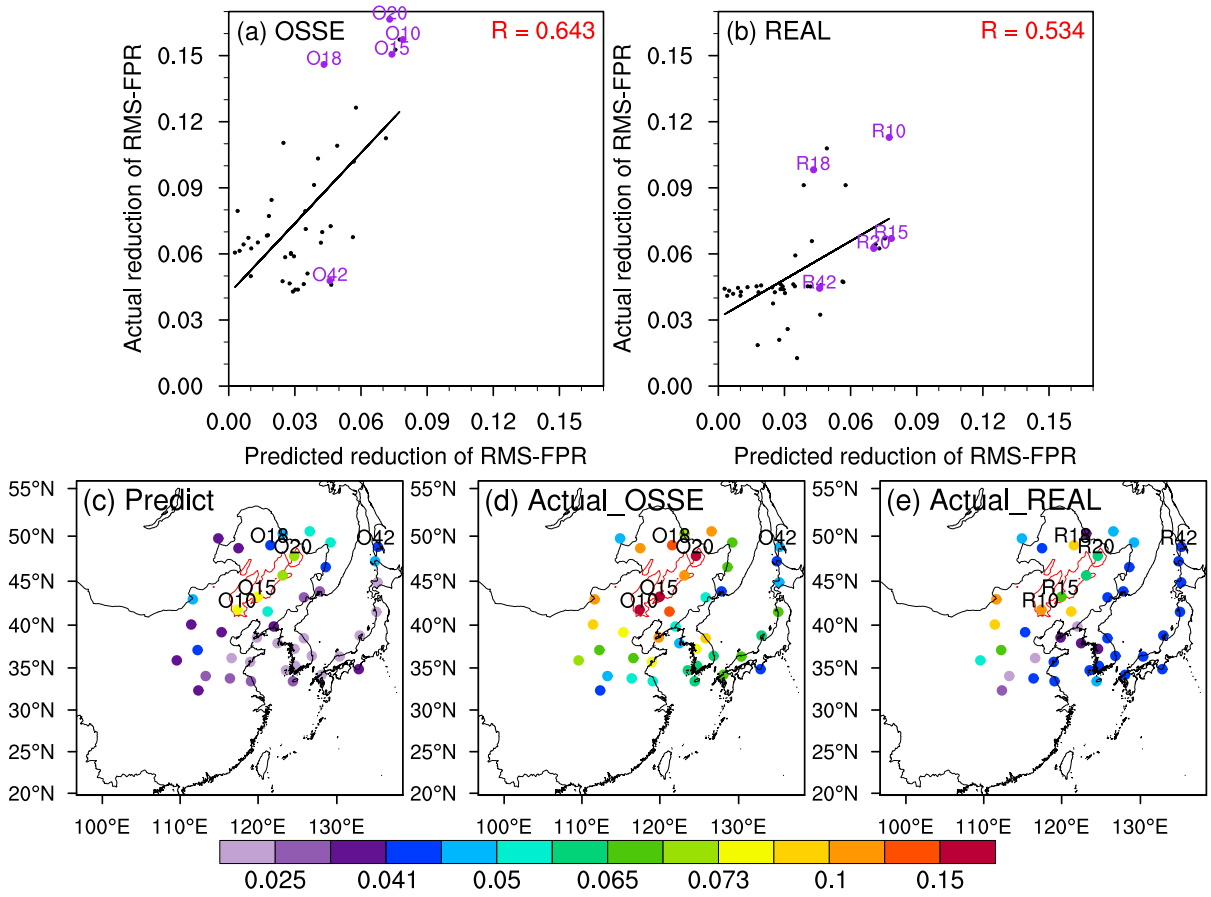

Fig. 10. (a, b) Scatterplot and linear regressions between predicted and actual reductions in the RMSE of the FPR in the verification region at the verification time for (a) OSSEs and (b) REALs, in which purple dots (10, 15, 20, 42, and 18) represent observation locations selected for special verification. (c–e) Spatial distributions of (c) predicted and actual reductions in the RMSE of the FPR for (d) OSSEs and (e) REALs, in which the red contour indicates that the value of the impact factor exceeds 0.505 (units: 10^{-2}) in Fig. 9b.

tions. This result indicates that if observations cannot be deployed at adaptive locations for practical reasons, deploying observations upstream as close as possible to adaptive locations can be considered a suboptimal option.

3.4.4.2. REALs

Results of the REALs are shown in Figs. 10b and e, Figs. 11b2–b6, and Figs. 12a2–c2. As we expected, the main results of the REALs are similar to those of the OSSEs: assimilating real observations in areas with larger predicted impact factors generally resulted in a better sea fog forecast performance than assimilating observations in areas with smaller predicted impact factors; the region with a large actual reduction in the RMSE of the FPR was generally located in the transition zone of the surface high–low system.

However, the correlation between the expected and actual reductions in the RMSE of the FPR for the REALs (Fig. 10b; value of 0.534) is much lower than that for the OSSEs (Fig. 10a; value of 0.643). Further analyses indicated that an important reason for the worse results of the REALs is the unexpectedly worse fog performance at some observation locations (such as R20; Fig. 11b4, Figs. 12a2–c2) in the region with both large expected and actual (OSSE) impact factors relative to other locations around the region with large expected impact factors (such as R18; Fig. 11b6, Figs. 12a2–c2). Considering the differences in experimental design between the OSSEs and REALs, this unexpectedly worse fog performance may result from certain actual adverse factors, such as observation and model errors (discussed in section 5). Thus, when assessing the actual benefits of adaptive observations for sea fog forecasts, the potential adverse impacts of actual factors cannot be ignored.

Overall, the results of both the OSSEs and REALs suggest that although the effectiveness of adaptive observations for fog forecasting is limited, the deployment of 850hPa-and-surface temperature in the transition region of the surface low–high system tends to yield greater benefits for improving forecasting of this fog event with the CFSP.

4. Verification based on another fog case with the CFSP

To verify the conclusions obtained based on the 2007 fog case, we selected another sea fog event, which occurred

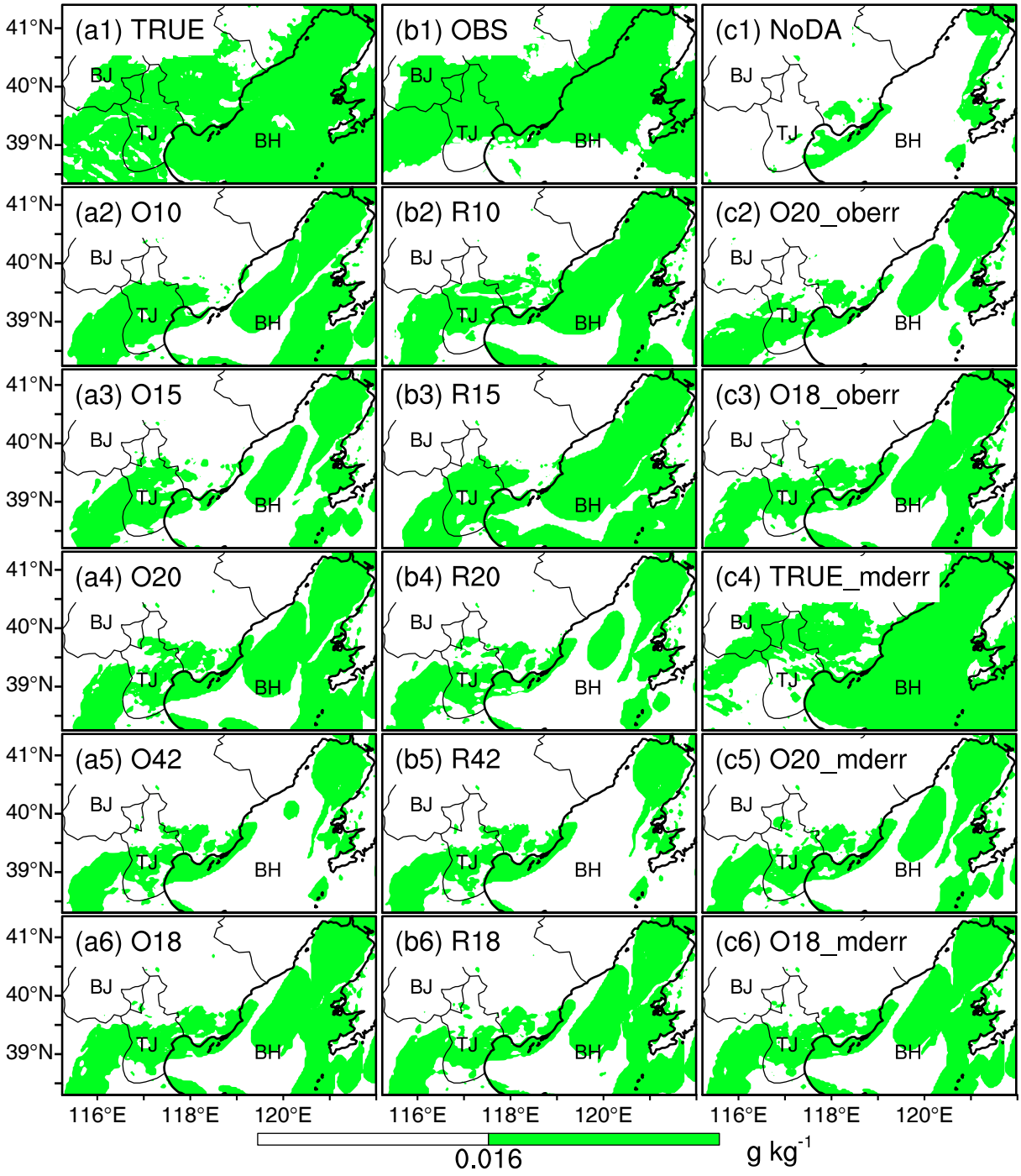

Fig. 11. As in Figs. 5d–k but for simulated fog coverage in the verification region (blue box in Figs. 5g and k) for the TRUE run (a1), NoDA (c1), OSSEs and REALs at locations 10, 15, 20, 42, and 18 (a2–a6 for OSSEs; b2–b6 for REALs), TRUE_modelerr run (c4), and additional OSSE experiments considering observation/model errors at locations 20 and 18 (c2–c3 for observation errors; c5–c6 for model errors), respectively, at the verification time.

from 3 to 4 March 2016 (hereinafter referred to as the 2016 fog case), also exhibiting CFSP characteristics [a detailed case overview is presented in Shi et al. (2018)]. At 0300 UTC 4 March 2016 (the mature stage of this fog event), fog was observed in most of the Bohai and Yellow seas (Fig. 13a). In this case, the deterministic run based on the FNL (DET_FNL) data could not capture this fog event well (Fig. 13b).

The experimental design of this fog case is the same as that of the 2007 fog case, as described in section 3.2, except for two points: first, to verify the effectiveness of adaptive observations, only REALs were conducted in this case instead of both OSSEs and REALs in the 2007 fog case; and second, REALs were performed by assimilating nine single 850hPa-and-surface temperature observations (the selec-

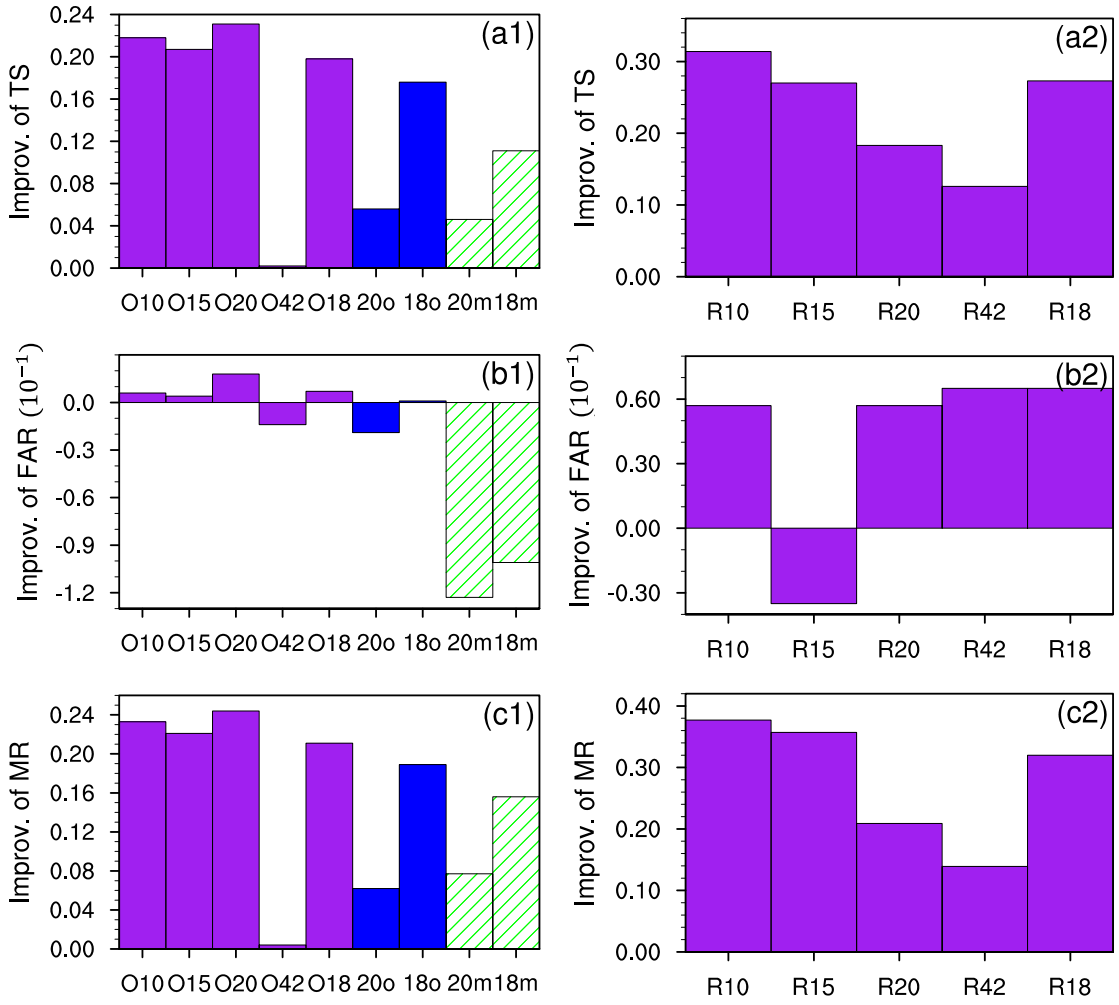

Fig. 12. Improvement of predictive skill scores (TS, FAR, and MR) between OSSEs and NoDA (purple bars in a1–c1), between additional OSSEs considering observation/model errors and NoDA (O20o, O18o for observation errors, blue bars in a1–c1; O20m, O18m for model errors, green bars in a1–c1), and between REALs and NoDA (a2–c2), respectively.

tion principle is documented in section 4.2) to save computing resources. ENS40_FNL was performed with the original initial time at 1200 UTC 2 March 2016 and was integrated for 48 h.

The times of 1200 UTC 3 March 2016 and 0300 UTC 4 March 2016 (the actual mature stage) were selected as the target time and verification time, respectively; the region marked by the blue box in Fig. 13 was defined as the verification region, with the same selection reason as those in the 2007 fog case.

4.1. *Predicted observation impact*

Generally, the predicted observation impacts in this case agree well with those in the 2007 fog case: the temperature at 850 hPa and the surface layer could be selected as the target observation type (Fig. 14). Additionally, the region with large expected observation impacts is located in the transition region of the surface low–high system, and the corresponding evolution is consistent with the main features of the CFSP (Figs. 15a–c).

4.2. *Effectiveness of adaptive observations*

Regarding the observations assimilated in the REALs, to ensure an as fair as possible verification in the case of limited observations used for verification, the observation location selection principle is as follows: first, establish the first location at the point with the largest predicted observation impact. Second, we regard the region with large predicted observation impacts at the target time as an ellipse and plot two perpendicular lines (the purple dashed lines in Fig. 15d), with both lines passing through the first location and one line approximately along the direction of the major axis of the ellipse. Finally, nine observations (including the first observation; marked with green circles in Fig. 15d) closest to these two lines are selected to conduct the REALs.

The results of the REALs (Fig. 16) generally agree with those of the 2007 fog case: both illustrated that adaptive observations at the identified adaptive locations provides some skill in actual targeting application for fog forecasting.

Overall, as both the 2007 and 2016 fog cases are typical

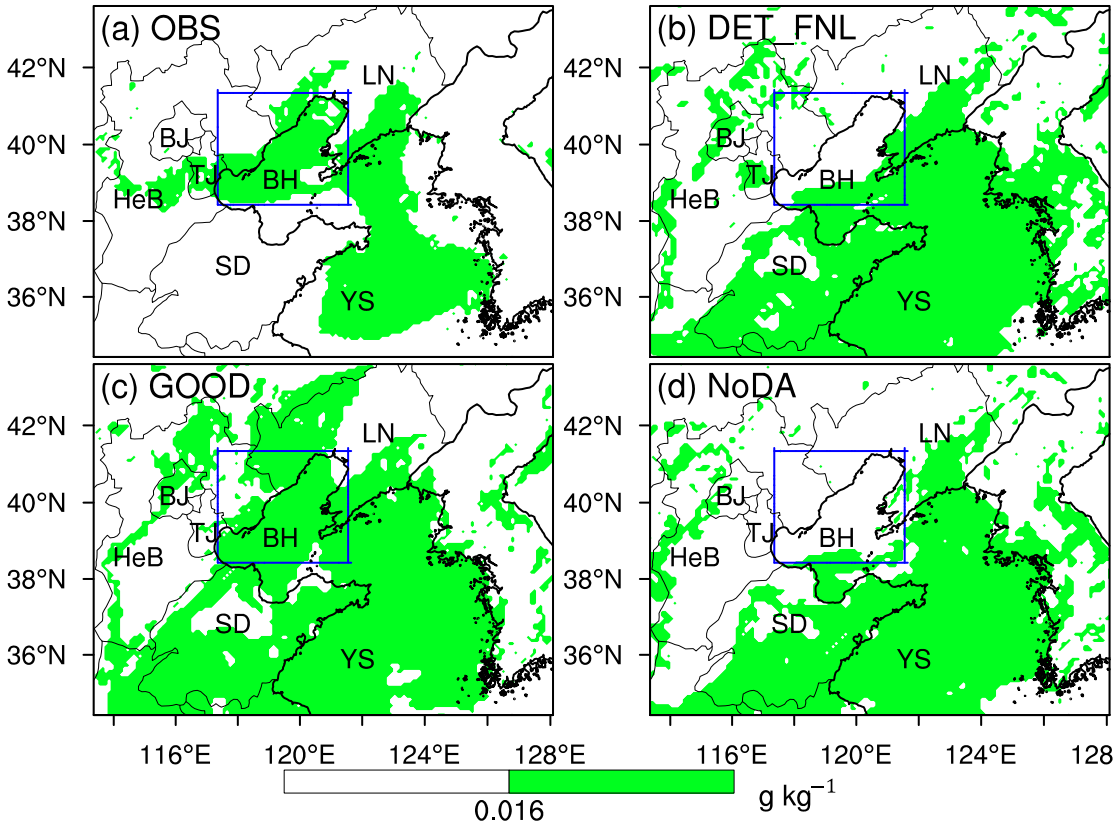

Fig. 13. As in Fig. 5 but for observed fog coverage detected by MTSAT data (a), and simulated fog coverage from (b) DET_FNL, (c) the TRUE run, and (d) the NoDA run, at 0300 UTC 4 March 2016 (verification time) for the 2016 fog case.

examples with CFSP features, the results of the 2016 fog case lend more credibility to the conclusions based on the 2007 fog case.

5. Impact of observation and model errors

Previous studies have indicated that observation errors constitute a potentially important source of the reduction in the effectiveness of adaptive observations (Morss and Emanuel, 2002; Xie et al., 2013). Additionally, it has been shown that fog forecasts are highly sensitive to model physical parameterization schemes, such as PBL schemes and shortwave/longwave radiation schemes (Tudor, 2010; Román-Cascón et al., 2012), which suggests that model errors exert a potentially adverse impact on the effectiveness of adaptive observations for fog forecasts. Thus, it could be determined that the results of the OSSEs (section 3.4.4.1) represent the upper limit of the effectiveness of adaptive observations for fog forecasting because they are conducted under the perfect-model assumption and involve the assimilation of synthetic observations without adding observation errors.

To explore the individual potential adverse impacts of observation and model errors on the effectiveness of adaptive observation for fog forecasts, two additional groups of sensitivity experiments (Exp_oberr and Exp_modelerr) were conducted on the basis of the OSSEs. Because this study does not focus on quantitatively comparing the influences of observation errors and model errors on fog forecasts, only five observation locations analyzed above—namely, locations 10, 15, 20, 42, and 18—were selected to conduct the sensitivity experiments. Locations 10, 15, and 20 represent locations with large expected impact factors; locations 18 and 42 represent locations upstream and close to areas with large expected impact factors and areas with small expected impact factors, respectively. In Exp_oberr, random errors proportional to the observation errors assigned by the WRF variational DA system (the same as used for the calculation of the expected impact factors in section 2) were added to the synthetic observations, which are directly obtained from the TRUE run. In the case of Exp_modelerr, synthetic observations were extracted from a new good run (hereafter referred to as the TRUE_modelerr run) without adding observation errors. The TRUE_modelerr run was generated with the same ICs as those of the TRUE run, but the physical parameterization schemes (PBL schemes and shortwave/longwave radiation schemes) were different from those of the TRUE run. Note that the results of Exp_oberr and Exp_modelerr were evaluated with the TRUE run and the TRUE_modelerr run as the reference, respectively.

The results of Exp_oberr and Exp_modelerr are shown in Fig. 17, Figs. 11c2 and c3, and Figs. 12c5 and c6. Both the observation and model errors caused a reduction in the

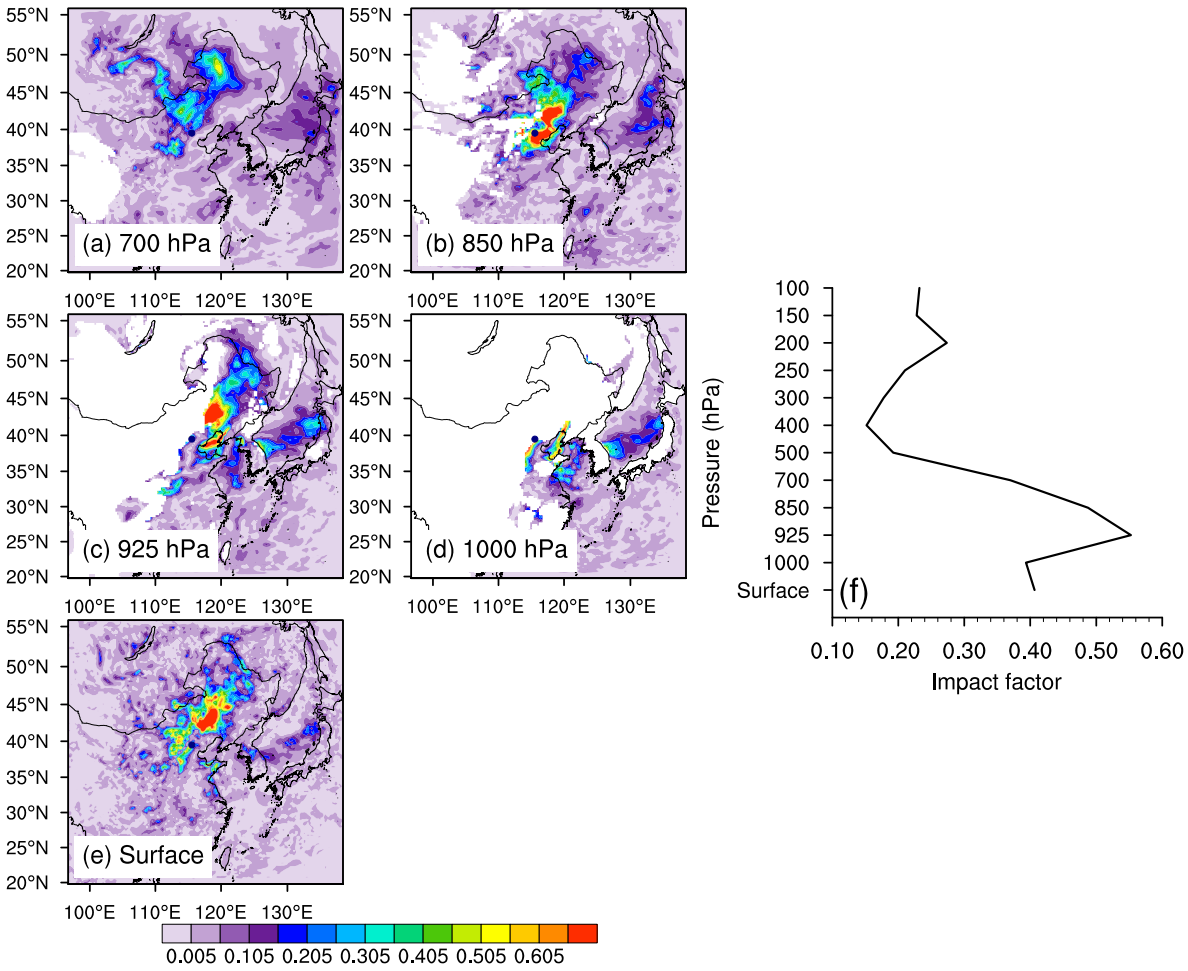

Fig. 14. (a–e) As in Figs. 8a2–e2 but for the impact factors of temperature at 1200 UTC 3 March 2016 (target time). (f) As in Fig. 7a but for temperature at the target time.

fog forecast performance. Additionally, the adverse actual impact of the observation (model) errors on the fog forecasts at the locations with different expected impact factors differed significantly: the adverse actual impact is largest at locations 20 and 10 (both with large expected impact factors), medium at location 18 (upstream of the area with large expected impact factors), and smallest at location 42 (with small expected impact factors). The possible reason is that the regions with the largest impact factors are also the regions with the fastest error growth (Xie et al., 2013). These results verified the speculation above that both observation and model errors could actually cause a reduction in the effectiveness of adaptive observations for sea fog forecasts, and emphasized the importance of improving the quality of observations and forecast models to improve the effectiveness of adaptive observations for fog forecasts.

6. Summary

In this study, we investigated the observation strategy and effectiveness of synoptic-scale adaptive observations for improving sea fog predictions by using the ESA method and WRF-EnKF model. A poorly predicted dense fog event, which occurred over the coastal region around the Bohai Sea on 21 February 2007 with a CFSP, was selected as a case in this study. By using the ESA method with the FPR, defined as the ratio of fog points (points with an LWC exceeding 0.016 g kg^{-1}) to the total points in the verification region, as a forecast metric, the impact factor (observation impact) was calculated to select the target observation type and to identify the corresponding adaptive locations. Then, the true observation impact given by the ESA method and the real effect of adaptive observation on fog forecasts were investigated by assimilating synthetic and real observations of target observation type, respectively. The results are concluded as follows:

(1) The 850 hPa-and-surface temperature was chosen as the target observation type.

(2) The transition region of the surface low–high systems were the identified adaptive locations. This region could be reasonably explained by the main features of the CFSP.

(3) Assimilating synthetic observations of target observation type at identified adaptive locations, on average, resulted in a larger actual reduction in fog forecast uncertain-

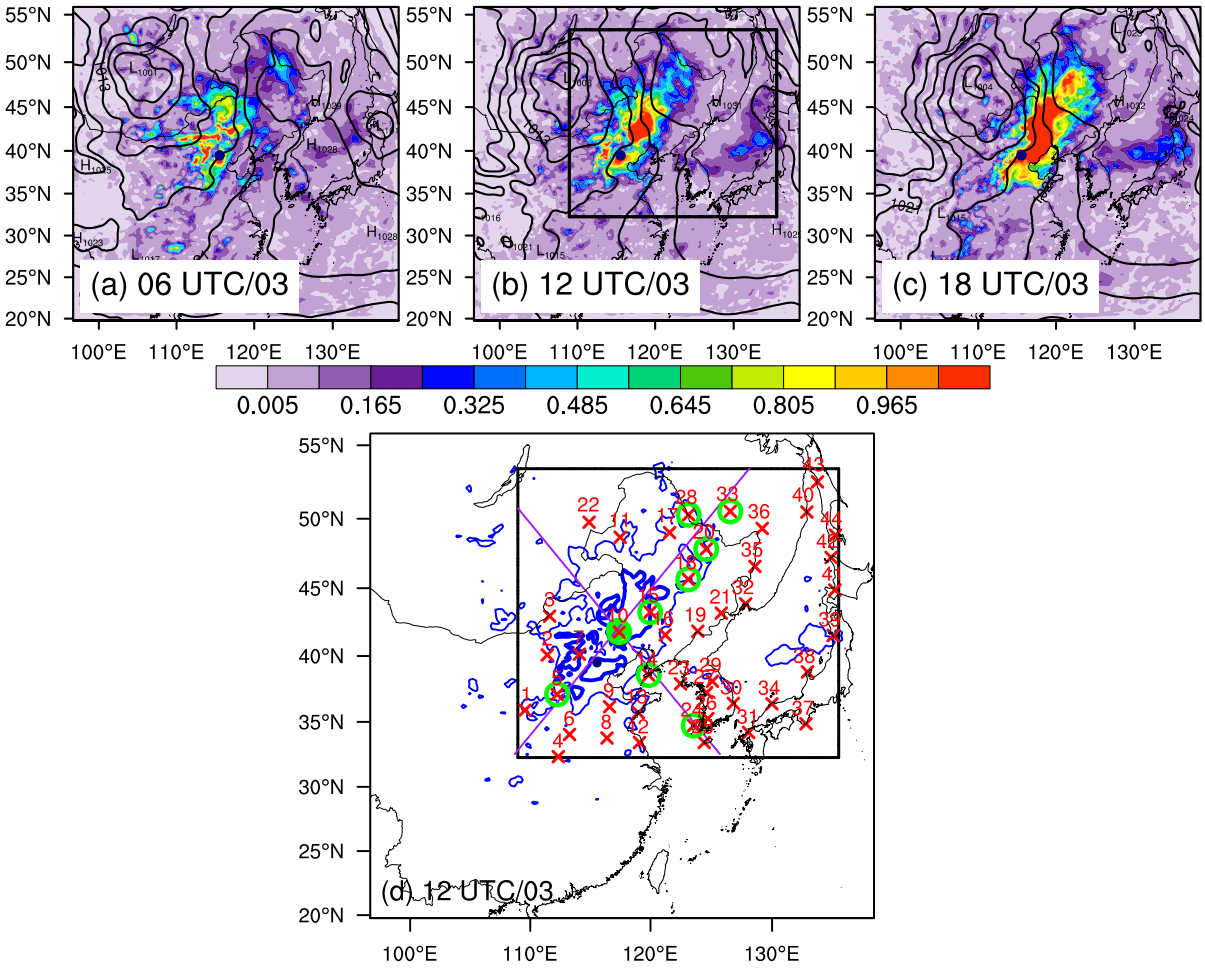

Fig. 15. (a–c) As in Fig. 9 but for the impact factor (units: 10^{-2}) at (a) 0600 UTC, (b) 1200 UTC, and (c) 1800 UTC on 3 March 2016. (d) Locations of all available real observations (red crosses) within the region of D_locate. Green circles indicate the locations of observations selected for the REALs. Purple dashed lines indicate directions along and perpendicular to the major axis of the approximate ellipse with one point passing through the location with the maximum predicted observation impact at 1200 UTC 3 March 2016. Thick and thin blue lines indicate the value of the impact factor exceeds 0.245 and 0.805, respectively.

ties than assimilating observations in other regions. Additionally, although the true effectiveness of adaptive observations given by the ESA method for fog forecasting was limited, it was still higher than that for TCs, which is possibly related to the relative strength of the nonlinearity in the governing dynamics between fog and TCs and different scales of forecast metrics adopted for fog and TC predictions.

(4) The real effectiveness of adaptive observations was reduced when real observations rather than synthetic observations were assimilated, which is possibly due to certain important actual factors, such as observation and model errors. This further indicates that reducing potentially important actual errors, such as observation and model errors, could be important for increasing the effectiveness of adaptive observations for fog forecasts in actual applications.

The main conclusions obtained from the 2007 fog case were verified by the 2016 fog case, which also exhibits the CFSP features. This further increases our confidence in actual targeting applications for adaptive observations of sea fog forecasts with a CFSP.

To the best of our knowledge, this is the first attempt at exploring the observation strategy and quantitatively assessing the effectiveness of adaptive observations for sea fog forecasting. This study extends the scope of atmospheric adaptive observations to fog systems. The advances obtained in this study could enhance our understanding of the predictability of fog with a CFSP and provide scientific guidance needed for implementing an observation network for fog forecasting in the coastal region around the Bohai Sea. Additionally, in this study, we investigated the effectiveness given by the ESA method for assimilating synoptic-scale adaptive observations for fog forecasting. Compared with previous studies using the same method, this method is more applicable to systems under a nearly linear error growth in the specified physical variables and forecast metrics related to larger-scale features. However, this study revealed two issues that require further investigation. First, as a potentially important observed variable, the role of the SST should be accounted for in

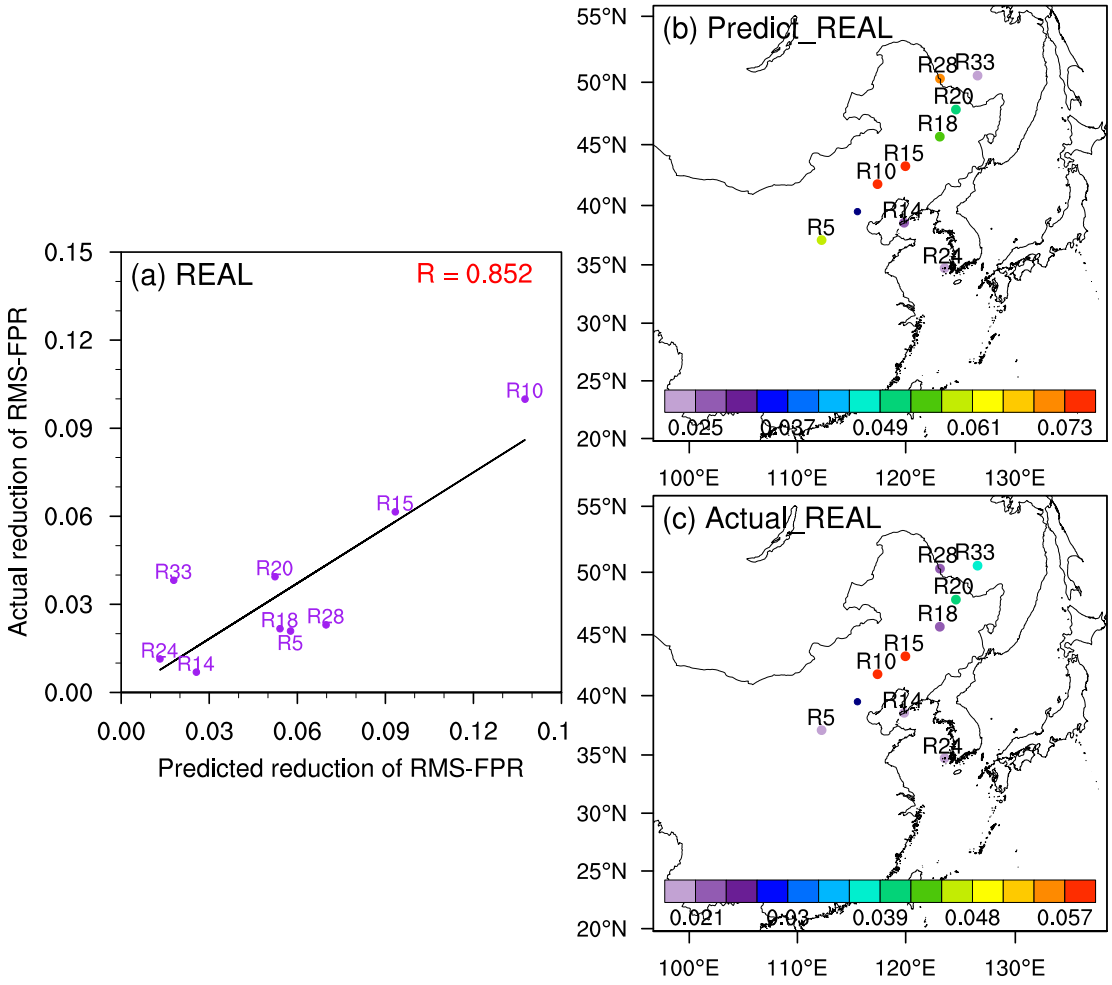

Fig. 16. As in Figs. 10b, c and e but for the 2016 fog case with locations as shown in Fig. 15d (green circles).

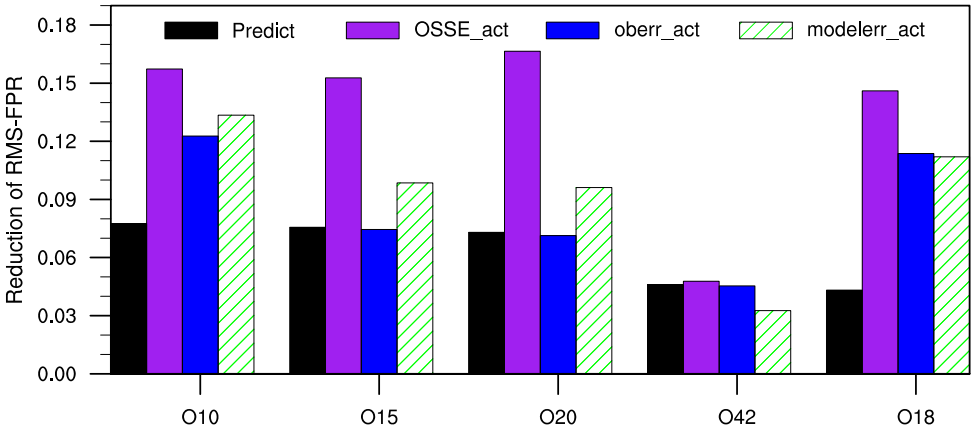

Fig. 17. Predicted (black) and actual reduction in the RMSE of the FPR for selected observations for OSSEs (purple), and sensitivity experiments considering observation errors (blue) or model errors (green) at different observation locations.

future work. Second, to expand our understanding of fog adaptive observations from the perspective of synoptic-scale circulations, studies should be conducted on other common synoptic scales, such as the rear-high synoptic pattern, over the Bohai Sea.

Acknowledgements. This study was supported by the National Natural Science Foundation of China (Grant No. 41705081), the Shandong Natural Science Foundation Project (Grant No. ZR2019ZD12), and the Laoshan Laboratory (Grant No. LSKJ202202203). The authors thank Juanzhen SUN from the

National Center for Atmospheric Research, and Yunji ZHANG from Pennsylvania State University for their helpful suggestions. We are also grateful to the data resources provided by Shanhong GAO from the Ocean University of China.

Data Availability Statement: The NCEP FNL reanalysis data are available online (https://rda.ucar.edu/datasets/ds083.2/). Real rawinsonde observation data were download from https://rda.ucar.edu/datasets/ds461.0/. The visibility observation data were obtained from the meteorological network of the China Meteorological Administration (http://www.cma.gov.cn/2011qxfw/2011qsjgx/). The MTSAT data were obtained from the network of Kochi University (http://weather.is.kochi-u.ac.jp). WRF source code and manuals were download from https://www2.mmm.ucar.edu/wrf/users/. WRF-EnKF source code was provided by the group of Professor Fuqing ZHANG, and can be download from https://github.com/huangynj/PSU_WRF_EnKF.

REFERENCES

Ancell, B., and G. J. Hakim, 2007: Comparing adjoint- and ensemble-sensitivity analysis with applications to observation targeting. *Mon. Wea. Rev.*, **135**, 4117–4134, https://doi.org/10.1175/2007MWR1904.1.

Bari, D., T. Bergot, and M. El Khlifi, 2015: Numerical study of a coastal fog event over Casablanca, Morocco. *Quart. J. Roy. Meteor. Soc.*, **141**, 1894–1905, https://doi.org/10.1002/qj.2494.

Bei, N. F., F. Q. Zhang, and J. W. Nielsen-Gammon, 2012: Ensemble-based observation targeting for improving ozone prediction in Houston and the surrounding area. *Pure Appl. Geophys.*, **169**, 539–554, https://doi.org/10.1007/s00024-011-0386-z.

Bishop, C. H., and Z. Toth, 1999: Ensemble transformation and adaptive observations. *J. Atmos. Sci.*, **56**, 1748–1765, https://doi.org/10.1175/1520-0469(1999)056<1748:ETAAO>2.0.CO;2.

Bishop, C. H., B. J. Etherton, and S. J. Majumdar, 2001: Adaptive sampling with the ensemble transform Kalman filter. Part I: Theoretical aspects. *Mon. Wea. Rev.*, **129**, 420–436, https://doi.org/10.1175/1520-0493(2001)129<0420:ASWTET>2.0.CO;2.

Buizza, R., and A. Montani, 1999: Targeting observations using singular vectors. *J. Atmos. Sci.*, **56**, 2965–2985, https://doi.org/10.1175/1520-0469(1999)056<2965:TOUSV>2.0.CO;2.

Dudhia, J., 1989: Numerical study of convection observed during the winter monsoon experiment using a mesoscale two-dimensional model. *J. Atmos. Sci.*, **46**, 3077–3107, https://doi.org/10.1175/1520-0469(1989)046<3077:NSOCOD>2.0.CO;2.

Gao, S. H., H. Lin, B. Shen, and G. Fu, 2007: A heavy sea fog event over the Yellow Sea in March 2005: Analysis and numerical modeling. *Adv. Atmos. Sci.*, **24**, 65–81, https://doi.org/10.1007/s00376-007-0065-2.

Glickman, T. S., 2000: *Glossary of Meteorology*. 2nd ed. American Meteorology Society, 855 pp.

Gultepe, I., and Coauthors, 2007: Fog research: A review of past achievements and future perspectives. *Pure Appl. Geophys.*, **164**, 1121–1159, https://doi.org/10.1007/s00024-007-0211-x .

Hamill, T. M., and C. Snyder, 2002: Using improved background-error covariances from an ensemble Kalman filter for adaptive observations. *Mon. Wea. Rev.*, **130**, 1552–1572, https://doi.org/10.1175/1520-0493(2002)130<1552:UIBECF>2.0.CO;2.

Hitt, K., 1994: Refining 1970's land-use data with 1990 population data to indicate new residential development. Water-Resources Investigations Report, 94–4250, https://doi.org/10.3133/wri944250.

Hong, S. Y., and J. O. J. Lim, 2006: The WRF single-moment 6-class microphysics scheme (WSM6). *Journal of the Korean Meteorological Society*, **42**, 129–151.

Hu, H. Q., J. Z. Sun, and Q. H. Zhang, 2017a: Assessing the impact of surface and wind profiler data on fog forecasting using WRF 3DVAR: An OSSE study on a dense fog event over North China. *J. Appl. Meteorol. Climatol.*, **56**, 1059–1081, https://doi.org/10.1175/JAMC-D-16-0246.1.

Hu, H. Q., Q. H. Zhang, B. G. Xie, Y. Ying, J. P. Zhang, and X. Wang, 2014: Predictability of an advection fog event over North China. Part I: Sensitivity to initial condition differences. *Mon. Wea. Rev.*, **142**, 1803–1822, https://doi.org/10.1175/MWR-D-13-00004.1.

Hu, H. Q., Q. H. Zhang, J. Z. Sun, C. Q. Ruan, F. Huang, and S. Q. Zhang, 2017b: Impact of high-frequency observations on fog forecasting: A case study of OSSE. *Tellus A: Dynamic Meteorology and Oceanography*, **69**, 1396182, https://doi.org/10.1080/16000870.2017.1396182.

Hu, H. Q., F. Huang, S. Q. Zhang, C. Q. Ruan, S. H. Gao, and P. Y. Li, 2019: Case study of fog predictability for an event with cold-front synoptic pattern. *Journal of Ocean University of China*, **18**, 271–281, https://doi.org/10.1007/s11802-019-3823-8.

Huang, B., D. Y. Mao, Z. M. Kang, Y. N. Cao, and C. Y. Xiang, 2011: Synoptic and climatic characteristics of Yellow Sea fog and causation analysis. *Journal of Tropical Meteorology*, **27**, 920–929, https://doi.org/10.3969/j.issn.1004-4965.2011.06.016.

Huang, L., and Z. Y. Meng, 2014: Quality of the target area for metrics with different nonlinearities in a mesoscale convective system. *Mon. Wea. Rev.*, **142**, 2379–2397, https://doi.org/10.1175/MWR-D-13-00244.1.

Kain, J. S., 2004: The Kain-Fritsch convective parameterization: An update. *J. Appl. Meteorol.*, **43**, 170–181, https://doi.org/10.1175/1520-0450(2004)043<0170:TKCPAU>2.0.CO;2.

Langland, R. H., 2005: Issues in targeted observing. *Quart. J. Roy. Meteor. Soc.*, **131**, 3409–3425, https://doi.org/10.1256/qj.05.130.

Langland, R. H., R. Gelaro, G. D. Rohaly, and M. A. Shapiro, 1999: Targeted observations in FASTEX: Adjoint-based targeting procedures and data impact experiments in IOP17 and IOP18. *Quart. J. Roy. Meteor. Soc.*, **125**, 3241–3270, https://doi.org/10.1002/qj.49712556107.

Li, P. Y., G. Fu, C. G. Lu, D. Fu, and S. Wang, 2012: The formation mechanism of a Spring sea fog event over the Yellow Sea Associated with a low-level jet. *Wea. Forecasting*, **27**, 1538–1553, https://doi.org/10.1175/WAF-D-11-00152.1.

Majumdar, S. J., 2016: A review of targeted observations. *Bull. Amer. Meteor. Soc.*, **97**(12), 2287–2303, https://doi.org/10.1175/BAMS-D-14-00259.1.

Majumdar, S. J., C. H. Bishop, B. J. Etherton, I. Szunyogh, and Z. Toth, 2001: Can an ensemble transform Kalman filter predict the reduction in forecast-error variance produced by targeted observations?. *Quart. J. Roy Meter. Soc.*, **127**,

2803–2820, https://doi.org/10.1002/qj.49712757815.

Majumdar, S. J., and Coauthors, 2011: Targeted observations for improving numerical weather prediction: An overview. WWRP/THORPEX Publication No. 15, 37 pp.

Mlawer, E. J., S. J. Taubman, P. D. Brown, M. J. Iacono, and S. A. Clough, 1997: Radiative transfer for inhomogeneous atmospheres: RRTM, a validated correlated-k model for the longwave. *J. Geophys. Res.: Atmos.*, **102** (D14), 16 663–16 682, https://doi.org/10.1029/97JD00237.

Morss, R. E., and K. A. Emanuel, 2002: Influence of added observations on analysis and forecast errors: Results from idealized systems. *Quart. J. Roy. Meteor. Soc.*, **128**, 285–321, https://doi.org/10.1256/00359000260498897.

Morss, R. E., K. A. Emanuel, and C. Snyder, 2001: Idealized adaptive observation strategies for improving numerical weather prediction. *J. Atmos. Sci.*, **58**, 210–232, https://doi.org/10.1175/1520-0469(2001)058<0210:IAOSFI>2.0.CO;2.

Mu, M., 2013: Methods, current status, and prospect of targeted observation. *Science China Earth Sciences*, **56**, 1997–2005, https://doi.org/10.1007/s11430-013-4727-x.

Mu, M., W. S. Duan, D. K. Chen, and W. D. Yu, 2015: Target observations for improving initialization of high-impact ocean-atmospheric environmental events forecasting. *National Science Review*, **2**, 226–236, https://doi.org/10.1093/nsr/nwv021.

Palmer, T. N., R. Gelaro, J. Barkmeijer, and R. Buizza, 1998: Singular vectors, metrics, and adaptive observations. *J. Atmos. Sci.*, **55**, 633–653, https://doi.org/10.1175/1520-0469(1998)055<0633:SVMAAO>2.0.CO;2.

Parrish, D. F., and J. C. Derber, 1992: The national meteorological center's spectral statistical-interpolation analysis system. *Mon. Wea. Rev.*, **120**, 1747–1763, https://doi.org/10.1175/1520-0493(1992)120<1747:TNMCSS>2.0.CO;2.

Román-Cascón, C., C. Yagüe, M. Sastre, G. Maqueda, F. Salamanca, and S. Viana, 2012: Observations and WRF simulations of fog events at the Spanish Northern Plateau. *Advances in Science and Research*, **8**, 11–18, https://doi.org/10.5194/asr-8-11-2012.

Shi, D. D., B. Huang, and Z. L. Wu, 2018: Analysis of atmosphere and sea characteristics under an obvious sea fog process over the Bohai and Yellow Sea in spring 2016. *Marine Forecasts*, **35**(5), 85–92, https://doi.org/10.11737/j.issn.1003-0239.2018.05.010. (in Chinese with English abstract)

Skamarock, W. C., and Coauthors, 2008: A Description of the Advanced Research WRF Version 3. NCAR Technical Note NCAR/TN-475+STR, 113 pp, https://doi.org/10.13140/RG.2.1.2310.6645.

Stuart, A. L., A. Aksoy, F. Q. Zhang, and J. W. Nielsen-Gammon, 2007: Ensemble-based data assimilation and targeted observation of a chemical tracer in a sea breeze model. *Atmos. Environ.*, **41**, 3082–3094, https://doi.org/10.1016/j.atmosenv.2006.11.046.

Sukoriansky, S., B. Galperin, and V. Perov, 2005: Application of a new spectral theory of stably stratified turbulence to the atmospheric boundary layer over sea ice. *Bound.-Layer Meteorol.*, **117**(2), 231–257, https://doi.org/10.1007/s10546-004-6848-4.

Torn, R. D., and G. J. Hakim, 2008: Ensemble-based sensitivity analysis. *Mon. Wea. Rev.*, **136**, 663–677, https://doi.org/10.1175/2007MWR2132.1.

Tudor, M., 2010: Impact of horizontal diffusion, radiation and cloudiness parameterization schemes on fog forecasting in valleys. *Meteorol. Atmos. Phys.*, **108**, 57–70, https://doi.org/10.1007/s00703-010-0084-x.

Wang, B. H., 1983: *Sea Fog*. China Ocean Press, Beijing, 330 pp.

Wang, Y. M., S. H. Gao, G. Fu, J. L. Sun, and S. P. Zhang, 2014: Assimilating MTSAT-derived humidity in nowcasting sea fog over the Yellow sea. *Wea. Forecasting*, **29**, 205–225, https://doi.org/10.1175/WAF-D-12-00123.1.

Xie, B. G., F. Q. Zhang, Q. H. Zhang, J. Poterjoy, and Y. H. Weng, 2013: Observing strategy and observation targeting for tropical cyclones using ensemble-based sensitivity analysis and data assimilation. *Mon. Wea. Rev.*, **141**, 1437–1453, https://doi.org/10.1175/MWR-D-12-00188.1.

Yang, Y., Y. M. Wang, S. H. Gao, and X. Y. Yuan, 2021: A new observation operator for the assimilation of satellite-derived relative humidity: Methodology and experiments with three sea fog cases over the Yellow Sea. *J. Meteor. Res.*, **35**, 1104–1124, https://doi.org/10.1007/s13351-021-1084-0.

Yue, J., and Z. Y. Meng, 2017: Impact of assimilating Taiwan's coastal radar radial velocity on forecasting Typhoon Morakot (2009) in southeastern China using a WRF-based EnKF. *Science China Earth Sciences*, **60**(2), 315–327, https://doi.org/10.1007/s11430-015-0259-y.

Zhang, C. L., S. G. Miao, Q. C. Li, and F. Chen, 2007: Impacts of fine-resolution land use information of Beijing on a summer severe rainfall simulation. *Chinese Journal of Geophysics*, **50**(5), 1172–1182, https://doi.org/10.1002/cjg2.1136.

Zhang, F. Q., 2005: Dynamics and structure of mesoscale error covariance of a winter cyclone estimated through short-range ensemble forecasts. *Mon. Wea. Rev.*, **133**(10), 2876–2893, https://doi.org/10.1175/MWR3009.1.

Zhang, F. Q., and J. A. Sippel, 2009: Effects of moist convection on hurricane predictability. *J. Atmos. Sci.*, **66**, 1944–1961, https://doi.org/10.1175/2009JAS2824.1.

Zhang, Y., Y. F. Xie, H. L. Wang, D. H. Chen, and Z. Toth, 2016: Ensemble transform sensitivity method for adaptive observations. *Adv. Atmos. Sci.*, **33**, 10–20, https://doi.org/10.1007/s00376-015-5031-9.

Zhou, B. B., 2011: Introduction to a new fog diagnostic scheme. NCEP Office Note 466, 43 pp.

Zhou, B. B., and B. S. Ferrier, 2008: Asymptotic analysis of equilibrium in radiation fog. *J. Appl. Meteorol. Climatol.*, **47**, 1704–1722, https://doi.org/10.1175/2007JAMC1685.1.